

The Milky Way's Rotation Curve to 60 kpc and an Estimate of the Dark Matter Halo Mass from Kinematics of ~ 2500 SDSS Blue Horizontal Branch Stars

X.-X. Xue^{1,2,3}, H.-W. Rix², G. Zhao¹, P. R. Fiorentin^{2,4}, T. Naab⁵, M. Steinmetz⁷,
F. C. van den Bosch², T. C. Beers⁶, Y. S. Lee⁶, E. F. Bell², C. Rockosi⁸, B. Yanny⁹,
H. Newberg¹⁰, R. Wilhelm¹¹, X. Kang², M. C. Smith¹², D. P. Schneider¹³

ABSTRACT

We derive new constraints on the mass of the Milky Way's dark matter halo, based on a set of halo stars from SDSS as kinematic tracers. Our sample contains 2466 rigorously selected Blue Horizontal-Branch (BHB) halo stars at $|z| \geq 4$ kpc and distances from the Galactic center up to ~ 60 kpc, with photometry and spectra drawn from SDSS DR-6. With distances accurate to $\sim 10\%$, this

¹The National Astronomical Observatories, CAS, 20A Datun Road, Chaoyang District, 100012, Beijing, China

²Max-Planck-Institute for Astronomy Königstuhl 17, D-69117, Heidelberg, Germany

³Graduate University of the Chinese Academy of Sciences, 19A Yuquan Road, Shijingshan District, 100049, Beijing, China

⁴Department of Physics, University of Ljubljana, Jadranska 19, 1000 Ljubljana, Slovenia

⁵Universität-Sternwarte München, Scheinerstr. 1, D-81679, München, Germany

⁶Department of Physics and Astronomy, CSCE: Center for the Study of Cosmic Evolution, and JINA: Joint Institute for Nuclear Astrophysics, Michigan State University, E. Lansing, MI 48824, USA

⁷Astrophysical Institute Potsdam, An der Sternwarte 16, 14482 Potsdam, Germany.

⁸Lick Observatory/University of California, Santa Cruz, CA 95060, USA

⁹Fermi National Accelerator Laboratory, P.O. Box 500 Batavia, IL 60510-5011, USA

¹⁰Department of Physics, Applied Physics, and Astronomy, Rensselaer Polytechnic Institute, Troy, NY 12180, USA

¹¹Department of Physics and Astronomy, Texas Tech University, Lubbock, TX 79409, USA

¹²Postal Address Institute of Astronomy, University of Cambridge, Madingley Road, Cambridge. CB3 0HA, United Kingdom

¹³Department of Astronomy and Astrophysics, 504 Davey Laboratory University Park, Pennsylvania 16802, USA

sample enables construction of the full line-of-sight velocity distribution at different Galactocentric radii. To interpret these distributions, we compare them to matched mock observations drawn from two different cosmological galaxy formation simulations designed to resemble the Milky Way, which we presume to have an appropriate orbital distribution of halo stars. Specifically, we select simulated halo stars in the same volume as the observations, and derive the distributions $P(V_{\text{l.o.s.}}/V_{\text{cir}})$ of their line-of-sight velocities for different radii, normalized by the simulation’s local circular velocity. We then determine which value of $V_{\text{cir}}(r)$ brings the observed distribution into agreement with the corresponding distributions from the simulations; these values are adopted as observational estimates for $V_{\text{cir}}(r)$ in the Milky Way’s halo. Subsequently, we apply a small correction, based on the Jeans Equation, to account for slight deviations in the radial density distribution of the simulated halo stars from the Milky Way’s actual stellar halo. This procedure results in an estimate of the Milky Way rotation curve to ~ 60 kpc, which is found to be slightly falling and implies $M(< 60 \text{ kpc}) = 4.0 \pm 0.7 \times 10^{11} M_{\odot}$. The radial dependence of the circular velocity, derived in statistically independent bins, is found to be consistent with the expectations from an NFW dark matter halo with the established stellar mass components at its center. If we assume an NFW halo profile of characteristic concentration holds, we can use the observations to estimate the virial mass of the Milky Way’s dark matter halo, $M_{\text{vir}} = 1.1 \pm 0.2 \times 10^{12} M_{\odot}$. We have checked that the particulars of the cosmological simulations are unlikely to introduce systematics larger than the statistical uncertainties. This estimate implies that nearly 40% of the baryons within the virial radius of the Milky Way’s dark matter halo reside in the stellar components of our Galaxy.

Subject headings: Milky Way: halo — Milky Way: dark matter — stars: blue horizontal branch stars

1. Introduction

The visible parts of galaxies are, in the current paradigm for galaxy formation, concentrations of baryons at the center of much larger dark matter halos, which have assembled through hierarchical merging and gas cooling. Understanding the properties of these dark matter host halos, their virial masses, concentration and radial mass profiles, *vis-a-vis* the luminous properties of the main galaxy at the center, is crucial for modelling the dynamics of the galaxy, for connecting observations of galaxies to large-scale cosmological dark matter

simulations, and for understanding what fraction of baryons in the halo ended up as stars in the galaxy. In turn, the extended stellar distributions of galaxies, in particular the stellar halos of nearby galaxies, offer some of the best probes to test generic predictions about the nature of dark matter mass profiles (Navarro et al. 1996).

Of course, the Milky Way and its surrounding halo are of particular interest, as our internal position permits placing unique constraints on the Galaxy’s stellar mass content, on its dark matter profile at large radii, and on the 3-D shape of its dark matter halo. Yet, our location within the Galaxy also complicates some measurements, such as the extended rotation curve of gas. As a result, the dark mass profile for the Milky Way between ~ 10 kpc and ~ 100 kpc and the halo’s virial mass are not constrained to better than a factor of 2-3. In practice, it has proven useful to quantify the halo mass profile by either a circular velocity curve, $V_{\text{cir}}(r)$, or by the escape velocity curve, $V_{\text{esc}}(r)$.

In previous work the most popular tools to estimate the Milky Way halo mass are the escape velocity and the velocity dispersion profile of the tracer population (i.e., halo stars, or the Milky Way’s satellite galaxies and globular clusters). The escape velocity provides constraints on the gravitational potential at the relevant position (Little & Tremaine 1987; Zaritsky et al. 1989; Kulessa & Lynden-Bell 1992; Kochanek 1996). Recent work has shown that the total mass of the halo is around $2 \times 10^{12} M_{\odot}$. Wilkinson & Evans (1999) used the velocities of 27 satellite galaxies and globular clusters to find a halo mass of $\sim 1.9^{+3.6}_{-1.7} \times 10^{12} M_{\odot}$ by adopting a truncated, flat rotation curve halo model; Sakamoto, Chiba & Beers (2003) used a sample including 11 satellite galaxies, 137 globular clusters, and 413 solar neighborhood field horizontal-branch stars, along with a flat rotation curve model, to obtain a total halo mass of $2.5^{+0.5}_{-1.0} \times 10^{12} M_{\odot}$ or $1.8^{+0.4}_{-0.7} \times 10^{12} M_{\odot}$, depending on the inclusion (or not) of Leo I. Recently, Smith et al. (2007) estimated a halo mass of $\sim 1.42^{+1.14}_{-0.54} \times 10^{12} M_{\odot}$, based on a sample of high-velocity stars from the RAVE survey and two published databases, and an adiabatically contracted NFW halo model; Battaglia et al. (2005; 2006) used a derived velocity dispersion profile to determine a total mass of $0.5 \sim 1.5 \times 10^{12} M_{\odot}$, with some dependence on the model adopted for the halo profile (see also Dehnen, McLaughlin & Sachania 2006).

In order to improve the precision of the mass estimate of the halo, the fundamental first step is to begin with high-quality data (tracers with accurate distances and radial velocities), augmented with an efficient method of analysis capable of extracting the maximum amount of information. For example, Wilkinson & Evans (1999) comment that a data set of ~ 200 radial velocities of BHB stars reduces the uncertainty in the mass estimate of the halo to $\sim 20\%$. This goal has proven elusive, even with data samples twice this size (e.g. Sakamoto et al. 2003), due to the use of a relatively nearby sample of tracers. However, we also expect

a large and distant data set to constrain the gravitational potential at different positions, which is ultimately a more reliable mass of the dark matter halo. The planned or already-underway kinematically unbiased surveys, such as the Global Astrometry Interferometer for Astrophysics (GAIA; Lindegren & Perryman 1996), the Space Interferometry Mission (SIM; Unwin et al. 2000), the RAdial Velocity Experiment (RAVE; Steinmetz et al. 2006), the Sloan Digital Sky Survey (SDSS; York et al. 2000), and the Sloan Extension for Galactic Understanding and Exploration (SEGUE; Newberg et al. 2003), will finally make it feasible to obtain the required large sample of tracers with well-measured parameters.

Blue Horizontal-Branch (BHB) stars are excellent tracers of Galactic halo dynamics, because they are luminous and have a nearly constant absolute magnitude within a restricted color range (see, e.g. Sirko et al. 2004 for BHB stars in SDSS). SDSS and SEGUE specifically targeted BHB stars for spectroscopy; we employ these stars (and other serendipitously discovered BHB stars with available spectra, e.g. mis-identified QSOs) to derive precision constraints on the mass of the Milky Way’s dark matter halo.

In Section 2 we describe the assembly of a particularly conservative (low contamination) selection of BHB stars from the spectra in SDSS DR-6. Two different cosmological simulations, one cosmological simulation of a galaxy resembling the Milky Way, with a $\sim 2 \times 10^{12} M_{\odot}$ halo, and one Milky-Way-like galaxy simulation with a $\sim 1 \times 10^{12} M_{\odot}$ halo, are presented in Section 3. This section also describes the estimation of the rotation curve, $V_{\text{cir}}(r)$, as a function of Galactocentric radius, obtained by comparing the observed BHB radial velocities to the kinematics of that simulation. In Section 4 we present the resulting estimates of rotation curve, and discuss the implication for the virial mass of the Milky Way’s halo. Our conclusions are summarized in Section 5.

2. Data

SDSS is an imaging and spectroscopic survey covering more than a quarter of the sky (York et al. 2000). Although its main focus was (and is) extragalactic science, there are still large numbers of stars not only imaged, but also targeted spectroscopically. In 2005 the project entered a new phase (SDSS-II), in which SEGUE, a sub-survey of SDSS-II, addresses fundamental questions about the formation and evolution of our own Galaxy (<http://www.sdss.org>). In addition to further (low-latitude) imaging, SEGUE in particular provides for a more systematic and extensive acquisition of spectroscopy for stars in the Milky Way, from which stellar parameters and radial velocities can be derived from the application of a well-calibrated and well-tested set of procedures, the SEGUE Stellar Parameter Pipeline (SSPP; see Lee et al. 2007a,b; Allende Prieto et al. 2007).

The Sloan Digital Sky Survey uses a CCD camera (Gunn et al. 1998) on a dedicated 2.5m telescope (Gunn et al. 2006) at Apache Point Observatory, New Mexico, to obtain images in five broad optical bands (*ugriz*; Fukugita et al. 1996). The survey data-processing software measures the properties of each detected object in the imaging data in all five bands, and determines and applies both astrometric and photometric calibrations (Lupton et al. 2001; Pier et al. 2003; Ivezić et al. 2004). Photometric calibration is provided by simultaneous observations with a 20-inch telescope at the same site (Hogg et al. 2001; Smith et al. 2002; Stoughton et al. 2002; Tucker et al. 2006). This work is based on stellar spectra that are part of the SDSS DR-6 (Adelman-McCarthy et al. 2008).

The radial velocities are taken from the SSPP, which (primarily) uses matches of the observed spectra to a set of 908 ELODIE template spectra, corrected to the heliocentric standard-of-rest (HSR) frame. Note that the SSPP automatically corrects for a systematic offset in SDSS stellar radial velocities of 7.3 km s^{-1} (see Lee et al. 2007a,b for derivation of this offset). After this correction is applied, the SDSS radial velocities exhibit negligible systematic errors, and have an accuracy between 5 and 20 km s^{-1} , depending on the S/N of the spectrum and the stellar spectral type.

2.1. Sample Selection

We aim to select as “pure” a set of true BHB stars as possible, where the contamination, e.g. from halo blue-straggler stars, is minimized, even if this selection procedure results in a smaller sample. We have not made any effort to construct a complete sample of BHB stars. Therefore, we have not simply followed the DR-6 classification procedures, but have employed a very stringent approach combining previously established color cuts with a set of Balmer-line profile selection criteria. Our technique is similar to that of Sirko et al. (2004), but we use slightly different in the adopted color cuts. Throughout this paper all magnitudes are corrected for Galactic extinction, and the colors are corrected for reddening, both based on the procedures of Schlegel et al. (1998).

2.1.1. Color Cuts

We start our selection of BHB stars by adopting the color cuts for identification of BHB candidates used in Yanny et al. (2000):

$$0.8 < u - g < 1.6$$

$$-0.5 < g - r < 0.0$$

These color cuts are shown in Figure 1. The rectangle is the region of BHB candidates. This color cut produces ~ 10000 BHB photometric candidates with existing spectra, but with a considerable contamination by both blue straggler (BS) stars and by warm main-sequence stars (MS). The subsequent spectroscopic analysis for BHB candidates is aimed at eliminating, or at least greatly reducing, contamination from such stars.

2.1.2. Balmer-Line Profile Cuts

BHB stars have lower surface gravities than BS stars and higher temperatures than MS stars. The Balmer-line profiles of warm stars are sensitive to both gravity and temperature; their analysis provides a powerful method to select BHB stars with confidence. We analyze the line profiles after normalizing the continuum for all stars, as illustrated in Figure 2. Then we combine two independent methods to identify non-BHB stars, as described below.

The $D_{0.2}$ *vs.* f_m method (Pier 1983; Sommer-Larsen, Christensen 1986; Arnold & Gilmore 1992; Flynn, Sommer-Larsen, & Christensen 1994; Kinman, Suntzeff, & Kraft 1994; Wilhelm, Beers, & Gray 1999), discriminates BHB stars from BS stars by determining the value of $D_{0.2}$, the width of the Balmer line at 20% below the local continuum, and distinguishes BHB stars from MS stars by measuring the value of f_m , the flux relative to the continuum at the line-core (Sirko et al. 2004). Figure 3 shows how $D_{0.2}$ can distinguish a BHB star from a BS star. A plot of $D_{0.2}$ versus f_m of the H_δ line for all stars passing the initial color cuts is shown in Figure 4. The concentration of stars centered at $(f_m, D_{0.2}) = (0.23, 25\text{\AA})$ represents the BHB stars; the stars with larger $D_{0.2}$ are BS stars, and the remaining stars are MS stars. Figure 4 implies the sample contamination resulting from the color-selection only is rather severe, on the order of 50%. The criteria for confirmation of a BHB star, based on the H_δ line analysis, are:

$$17 \text{ \AA} \leq D_{0.2} \leq 28.5 \text{ \AA}, \quad 0.1 \leq f_m \leq 0.3 .$$

The *scale width vs. shape* method (Clewley et al. 2002) is based on a Sérsic profile (Sérsic 1968) fit to the Balmer lines:

$$y = 1.0 - a \exp \left[- \left(\frac{|\lambda - \lambda_0|}{b} \right)^c \right], \quad (1)$$

where y is the normalized flux density and λ_0 is assumed to be the nominal wavelength of the Balmer line. To account for small radial velocity corrections and the imperfect normalization

of spectra, we fit the normalized extracted spectrum to the Sérsic profile with five free parameters : a, b, c, λ_0 and n .

$$y = n - a \exp \left[- \left(\frac{|\lambda - \lambda_0|}{b} \right)^c \right] \quad (2)$$

The set of stars that passed the initial color cuts exhibits a bimodal distribution in the c_γ versus b_γ plane (Figure 5), where γ refers to the H_γ line. This gap allows one to quite cleanly separate BHB stars from BS stars, according to:

$$0.7 \leq c_\gamma \leq 1.25$$

$$7 \text{ \AA} \leq b_\gamma \leq 10.8 - 26.5 (c_\gamma - 1.08)^2 \text{ .}$$

As the color coding of the points in Figure 5 shows, most BHB stars selected by the $D_{0.2}$ & f_m method already lie in the appropriate region of the *scale width vs. shape* method applied to H_γ . The combination of these two stringent criteria indeed appears to eliminate most stars that are not *bona-fide* BHB stars. The combination of Figure 4 and Figure 5 suggests that the contamination is well below 10%.

There are a total of 2625 stars that survive the color cuts, and *both* of the Balmer-line profile cuts described above. This sample forms the basis of our remaining analysis.

2.2. The Absolute Magnitude of BHB Stars

Our basic approach is to identify BHB stars from their spectra (Section 2.1), then estimate their absolute magnitude from photometry alone. BHB stars have similar, but not identical, absolute magnitudes, as they are affected slightly by temperature and metallicity (e.g. Wilhelm, Beers, & Gray 1999; Sirko et al. 2004). Figure 6 shows five theoretical absolute magnitudes $M_g = 0.60, 0.55, 0.65, 0.70, 0.80$ in the $(u - g, g - r)$ plane, taken from Sirko et al. (2004). For each BHB star in our sample we define the most probable absolute magnitude associated with its $(u - g, g - r)$ colors by simply finding the absolute magnitude of the point on the theoretical track that is closest to the observed star in this color-color space. The absolute magnitude error of a given star derived from this method is on the order of 0.2 mag (Sirko et al. 2004), corresponding to a distance accuracy of 10%; errors in the measured photometry are much smaller than this error. The distance from the Sun, and from the Galactic center can then be determined from:

$$g = M_g + 5 \log_{10} d - 5 \quad (3)$$

$$r^2 = (R_\odot - d \cos(b) \cos(l))^2 + d^2 \sin^2(b) + d^2 \cos^2(b) \sin^2(l), \quad (4)$$

where g is the extinction-corrected magnitude in the g band, M_g is the absolute magnitude in the g band, d is the distance to the Sun, r is the distance from the Galactic center, b is the Galactic latitude, and l is the Galactic longitude; we take R_\odot to be 8.0 kpc.

2.3. The Spatial, Velocity and Metallicity Distribution of the BHB Star Sample

For ease of the subsequent analysis, we convert the heliocentric radial velocities to the Galactic standard of rest (GSR) frame by adopting a value of 220 km s^{-1} for the Local Standard of Rest and a Solar motion of $(+10.0, +5.2, +7.2) \text{ km s}^{-1}$ in (U, V, W) , which are defined in a right-handed Galactic system with U pointing towards the Galactic center, V in the direction of rotation, and W towards the north Galactic pole (Dehnen & Binney 1998). Hereafter $V_{\text{l.o.s}}$ stands for the radial velocity in the GSR frame (i.e., the radial velocity component along the star-Sun direction, corrected for Galactic rotation). If V_{helio} is the heliocentric radial velocity, then:

$$V_{\text{l.o.s}} = V_{\text{helio}} + 10.0 \text{ km s}^{-1} \times \cos(l) \cos(b) + 7.2 \text{ km s}^{-1} \times \sin(b) + 225.2 \text{ km s}^{-1} \times \sin(l) \cos(b). \quad (5)$$

Our sample of 2625 BHB stars may contain some thick-disk stars, with $1 \text{ kpc} < |z| < 4 \text{ kpc}$, so we impose an additional geometric constraint $|z| > 4 \text{ kpc}$, which reduces the sample to 2466 (presumed) *halo* BHB stars within 60 kpc and with radial velocity error less than 30 km s^{-1} .

The spatial distribution of our 2466 halo BHB stars is shown in Figure 7 and Figure 8, with all stars located at least 4 kpc from the Galactic disk and at 5 – 60 kpc from the Galactic center. The observed distribution of line-of-sight velocities is well-fit by a Gaussian distribution with $\sigma_{v_{\text{l.o.s}}} = 106 \text{ km s}^{-1}$, as shown in the upper panel of Figure 9. Figure 9(lower panel) shows the derived $[\text{Fe}/\text{H}]$ estimates for the BHB sample reported by the SSPP (see Lee et al. 2007a,b for details). Most of our BHB stars are metal-poor ($[\text{Fe}/\text{H}] \sim -2$), as expected

for a sample of halo stars. This is further test to the quality of the SDSS spectra and the rigor of the sample selection. The upper panel of Figure 10 shows the distribution of $V_{l.o.s}$ vs r for the entire sample. It reveals a nearly equal number of stars with positive and negative $V_{l.o.s}$ at a given radius: the BHB population exhibits very little net rotation, so we will subsequently analyze only $V_{l.o.s}$. The lower panel of Figure 10 shows the binned velocity dispersion, $\sigma_{l.o.s}$, of the sample as a function of radius. It is well described by $\sigma(r) = 112 \text{ km s}^{-1} \times e^{\frac{-r}{322 \text{ kpc}}}$, which we will subsequently use in Jeans Equation modelling. The radial number density profile of halo stars in the Milky Way in the range $\sim 10 - 60$ kpc can be approximated by $\rho \sim r^{-3.5}$ (e.g. Bell et al 2007). Accounting for the $r^2 dr$ volume effect, inspection of Figure 10 and Figure 12 shows that the radial distribution of our BHB sample falls off much more rapidly than this, in particular at large distances. This is mostly attributable to the SDSS spectroscopic target selection. The chances of a candidate BHB star to be targeted for spectroscopy in the course of SDSS and SEGUE is not a simple function of its apparent magnitude, but depends on many, often operational factors, which have also evolved over the course of the survey. The net result is that only under very favorable circumstances are distant (hence faint) BHB's get targeted, and had spectra obtained that were of sufficient S/N to pass our quality criteria. As a result, the radial distribution of our sample falls off much more steeply than the parent population of halo BHB stars. We account for these effects in the subsequent analysis.

Overall, our present sample of distant halo stars with available kinematics is nearly an order of magnitude larger than that of Battaglia et al. (2005), which has 240 stars. Because our tracers are BHB stars, their distances are also known more accurately. However, the Battaglia et al. sample extends to larger radii, ~ 100 kpc.

3. Modeling the BHB Kinematics

We now describe our approach to convert the $V_{l.o.s}(r)$ measurements for the ~ 2500 BHB stars into estimates of $V_{\text{cir}}(r)$ of the Milky Way halo, and ultimately to estimate M_{vir} for the Milky Way's halo. With the full line-of-sight velocity data set, sampling radii of $5 - 60$ kpc, we can obtain both the velocity dispersion, $\sigma_{l.o.s}$, and identify a set of exceptionally high-velocity stars at various radii that might be suitable to estimate $V_{\text{esc}}(r)$. Some previous work (e.g. Battaglia et al 2005) considered only velocity dispersions, while others focused only on high-velocity stars in the Solar neighborhood (Sakamoto et al. 2003; Smith et al. 2007). We will consider the full velocity distribution; as we shall see later, it is close to a Gaussian and hence most information is contained in $\sigma_{l.o.s}$.

To link the observables, $V_{l.o.s}$ and r to $V_{\text{cir}}(r)$, we must not only account for the particular

survey volume, but also need to make at least an implicit assumption about the nature of the halo-star distribution function, in particular its (an-)isotropy. In contrast to, e.g. Battaglia et al. (2005), we restrict ourselves not only to Jeans Equation modelling, but choose to account for these issues also by resorting to a comparison with the cosmologically motivated galaxy simulations, to make “mock observations” within these simulations, and then match test results to the observations. One cannot expect the halo stars in the simulations to have exactly the sample density profile as the actual stars in the halo of the Milky Way; we account for such differences as described below.

3.1. Halo Star Kinematics in Simulated Galaxies

Based on prior estimates of the halo mass, we chose two SPH simulations corresponding to the formation of a Milky Way-like $\sim 2 \times 10^{12} M_{\odot}$ halo, and a $\sim 1 \times 10^{12} M_{\odot}$ halo (T. Naab and M. Steinmetz, private communication), from which “pseudo-observations” are constructed for comparison with the data.

The first cosmological simulation of the halo used for this study is presented in detail in Naab et al. (2007): their ‘halo A’ at 100^3 resolution. This isolated halo was picked from a low-resolution cosmological dark matter simulation ($\Omega_0 = 0.3$, $H_0 = 65 \text{ km s}^{-1} \text{ Mpc}^{-1}$, baryon fraction $f_b = 0.2$), and re-simulated at higher resolution. The simulation was followed using GADGET-2 (Springel 2005) and a standard star-formation prescription (Springel et al. 2003), but without stellar feedback. Using an overdensity threshold of $\delta_c = 340$, the simulated halo had a present-day virial radius of $r_{\text{vir}} = 345 \text{ kpc}$, and a virial mass of $M_{\text{vir}} = 2.1 \times 10^{12} M_{\odot}$ (these values differ from Naab et al. 2007, as we use a different virial contrast in this paper).

The individual particle masses were $m_{\text{star}} = 8.3 \times 10^6 M_{\odot}$ and $m_{\text{halo}} = 6.6 \times 10^7 M_{\odot}$ for the stars and the dark matter particles, respectively. This resulted in 2.2×10^5 star particles and 2.0×10^5 halo particles within the virial radius. The stellar gravitational softening length was $\epsilon_{\text{star}} = 0.25 \text{ kpc}$. For further details see Naab et al. (2007).

The second cosmological simulation of the halo used for this study is one with a $\sim 10^{12} M_{\odot}$ halo, following the prescriptions of Abadi et al. (2003).

From these simulations for each particle we have the 3-D positions and 3-D velocities, the circular velocity $V_{\text{cir}} \equiv \sqrt{r \partial \Phi / \partial r}$, and the escape velocity V_{esc} to the virial radius of the simulation at each given position. Because SDSS/SEGUE only observed $\approx \pi$ steradians, not the entire sky (see Figure 11), to compare the observations to the simulations we must select simulated star particles in the same region as the SDSS footprint.

As a first step, we specified “Galactic coordinates” in the simulation by defining the “Galactic Plane” by the net angular momentum of all (stellar) particles within 10 kpc of the center. In this coordinate system one has (by definition) $\vec{L}_{tot} = |\vec{L}_{tot}|\vec{e}_z$, and the Sun is at $(x_\odot, y_\odot, 0.0)$ kpc ($R_\odot = \sqrt{x_\odot^2 + y_\odot^2} = 8.0$ kpc). We can then calculate the Galactocentric radial velocity as seen from the “Sun” for each simulation particle as:

$$d = \sqrt{(x - x_\odot)^2 + (y - y_\odot)^2 + z^2}$$

$$v_{l.o.s} = \frac{v_x(x - x_\odot) + v_y(y - y_\odot) + v_z z}{d} \quad (6)$$

To create “pseudo-observations”, firstly we remove the satellites in the simulation and then assume 10 positions for the Sun that all have $R=8$ kpc and $z=0$ kpc but different azimuthal angles ϕ . The corresponding RA and DEC in this coordinate system can then be used to select the star particles in the same region of the simulation as our observed BHB sample. The effective flux limit of the BHB sample, $g \leq 20$, implies a maximum distance from the Sun of about 76 kpc, a distance which we impose as a selection limit in the simulations. To select “halo” stars, we also impose that the stars have to be at least 4 kpc above or below the disk plane. Finally, we average these 10 samples of simulated halo stars. Figure 11 shows the distribution of these selected simulated stars and the observed halo BHB stars in RA and DEC.

This procedure results in a sample of simulated halo stars (each position produces an “observational dataset”) with Galactocentric radial velocities, Galactocentric radii, escape velocities, and circular velocities, whose distribution is shown in Figure 12. This Figure makes it clear that, even in a large sample, the Galactocentric radial velocity rarely approaches the escape velocity (one obvious reason being that we measure only the projected component of the space velocity).

3.2. Estimating $V_{cir}(r)$ from the data

We analyze the implications of the observed BHB kinematics for the Milky Way halo’s mass distribution in two steps. We first estimate $V_{cir}(r)$ from the data-simulation comparison in a set of statistically independent radial bins, effectively constructing a circular velocity curve extending to 60 kpc. Then we fit the circular velocity curve with NFW halo models (and bulge+disk) resulting in estimates of M_{vir} , where it must be noted that the Milky Way halo’s presumed virial radius extends about a factor of four beyond the farthest BHB stars in the sample.

For the data-model comparison we construct the distributions of $P(V_{\text{l.o.s.}}/V_{\text{cir}}(r))$ for the simulations and then scale the observed $P_{\text{obs}}(V_{\text{l.o.s.}})$ at that radius by the value of V_{cir} that best matches the simulated distribution. In practice, we divide the Galactocentric radius (r) into 10 bins and apply this test, resulting in 10 (statistically) independent radial estimates of $V_{\text{cir}}(r)$. Specifically, the bins we adopted were 5–10 kpc, 10–15 kpc, 15–20 kpc, 20–25 kpc, 25–30 kpc, 30–35 kpc, 35–40 kpc, 40–45 kpc, 45–50 kpc, and 50–60 kpc, all in distance from the Galactic Center, not from the Sun. The quality of the match is evaluated from a Kolmogorov-Smirnov test probability that both distributions were drawn from the same parent population. This approach to estimating $V_{\text{cir}}(r)$ is illustrated in Figure 13. In this Figure, the red line shows $P(V_{\text{l.o.s.}}/V_{\text{cir}})$ from Naab’s simulation, while the black line shows $P_{\text{obs}}(V_{\text{l.o.s.}})$, scaled to an estimated escape velocity of 163 km s^{-1} . The entire velocity distribution fits remarkably well.

In a given gravitational potential, more centrally concentrated kinematic tracer populations will exhibit smaller velocity dispersions than more extended ones. In the simple case of a spherical potential, with tracers of $\rho \sim r^{-\gamma}$ and an isotropic velocity dispersion that varies only slowly with radius, the Jeans Equation, for a given $V_{\text{cir}}(r)$, yields the relative velocity dispersions of the two populations, $\sigma_1/\sigma_2 = \sqrt{\gamma_2/\gamma_1}$, where the indices refer to two different hypothetical tracer populations.

In the radial range of 10-60 kpc, the density profile of Naab’s simulated halo stars is approximately $\rho \sim r^{-2.9}$, while that of Steinmetz’s simulation is $\sim \rho \sim r^{-3.7}$. This, however, should not be compared to the radial distribution of the stars for which we actually have velocities, but to the radial profile of halo stars from which they were drawn (see Section 2.3). This requires the reasonable assumption that the measured velocities are uncorrelated to the spectral targeting, i.e., even a more complete sampling of BHB stars at a given radius would have yielded the same velocity distribution. As an estimate for the actual density profile for the Milky Way’s stellar halo at 10-60 kpc, we take the estimates (for main sequence turn-off stars) of $\rho \sim r^{-3.5}$ (Bell et al. 2007), based on SDSS. Using the above correction based on the Jeans Equation, we must subsequently revise the derived velocity scales for the Milky Way halo upward by $\sqrt{3.5/2.9} = 1.1$ for Naab’s simulation and downward by $\sqrt{3.5/3.7} = 0.97$ for Steinmetz’s simulation.

Matching $P(V_{\text{l.o.s.}}/V_{\text{cir}}(r))$, and applying the above correction, we obtain the estimates summarized in Figure 14 and in Table 1. The filled circles in this Figure reflect the $V_{\text{cir}}(r)$ estimates based on Steinmetz’s simulation, while the filled squares stand for the $V_{\text{cir}}(r)$ estimates based on Naab’s simulation. To estimate the statistical uncertainties on these values, we use bootstrap resampling on our BHB sample (typically 100 times), repeat the above procedure, and indicate the resulting 68% (one-sigma) confidence region as error bars.

For reference, we show how these estimates of $V_{\text{cir}}(r)$ compare to those derived from the Jeans Equation and the fit to $\sigma_{\text{l.o.s}}(r)$ shown in Figure 10. From the Jeans Equation, $V_{\text{cir}}(r)$ can be estimated from the velocity dispersion, σ_r (Binney & Tremaine 1987),

$$\frac{r}{\rho} \frac{d(\sigma_r^2 \rho)}{dr} - 2\beta \sigma_r^2 = V_{\text{cir}}^2(r) \quad (7)$$

with

$$\beta = 1 - \frac{\sigma_t^2}{\sigma_r^2} \quad (8)$$

where $\sigma_r(r)$ and $\sigma_t(r)$ are the radial and tangential velocity dispersions, respectively, in spherical coordinates, $\rho(r)$ is the stellar density.

The distribution of the halo stars in the simulations are in anisotropic, with $\beta = 0.37$, and the simulations exhibit $\sigma_{\text{l.o.s}}(r) \approx \sigma_r(r)$ for this particular survey volume. Taking from Figure 10 the fit to $\sigma_{\text{l.o.s}}(r)$ of the BHB stars, $\sigma_{\text{l.o.s}}(r) = 112 \text{ km s}^{-1} \times e^{\frac{-r}{322 \text{ kpc}}}$, and assuming $\sigma_{\text{l.o.s}}(r) \approx \sigma_r(r)$ for BHB stars, we can derive two circular velocity curves, for $\beta = 0.37$ (anisotropic), and $\beta = 0$ (isotropic), respectively, by adopting $\rho(r) \sim r^{-3.5}$ (see Figure 14). They both agree well with the simulation-based estimates.

4. Results

Figure 15 and Figure 16 present the central result of our analysis, $V_{\text{cir}}(r)$, an estimate of the rotation curve from $\sim 10 - 60 \text{ kpc}$. This represents the first time that the rotation curve for the Galaxy has been estimated to such large distances at this accuracy. Note that at small radii this estimate, though derived from halo stars, agrees well (within $\sim 10\%$) with established determinations at the Solar radius ($\sim 220 \text{ km s}^{-1}$). Beyond the Solar radius, the rotation curve appears to be gently falling to 175 km s^{-1} at $\sim 60 \text{ kpc}$. Note also that the circular velocity curve is a conceptually more robust estimate than V_{esc} , which depends more sensitively than V_{cir} on $\Phi(r)$ at radii beyond the measurements.

Using the functional form for $V_{\text{cir}}(r)$ expected for an NFW halo and the stellar component (see below) just as a means to interpolate the individual rotation curve estimates, one obtains $V_{\text{cir}}(60 \text{ kpc}) = 175 \pm 15 \text{ km s}^{-1}$, or $M(< 60 \text{ kpc}) = 4.0 \pm 0.7 \times 10^{11} M_{\odot}$.

This is the largest radius at which the data directly constrain $V_{\text{cir}}(r)$ or $M(< r)$. Yet this radius is only $1/3$ of the expected virial radius of the Milky Way’s halo. We therefore proceed with a separate step, to use these $V_{\text{cir}}(r)$ estimates to constrain parameterized models for the overall dark matter halo. We adopt a spherical Hernquist (1990) bulge and an exponential

disk for the stellar components and describe the halo by an NFW profile (Navarro et al. 1996). The total potential can then be simply expressed as

$$\Phi_{\text{tot}}(r) = \Phi_{\text{disk}}(r) + \Phi_{\text{bulge}}(r) + \Phi_{\text{NFW}}(r), \quad (9)$$

with an assumed potential, presumed to be spherically symmetric, for the disk and bulge of

$$\Phi_{\text{disk}}(r) = -\frac{GM_{\text{disk}}(1 - e^{-\frac{r}{b}})}{r}, \quad (10)$$

$$\Phi_{\text{bulge}}(r) = -\frac{GM_{\text{bulge}}}{r + c_0}, \quad (11)$$

where $M_{\text{bulge}} = 1.5 \times 10^{10} M_{\odot}$, $c_0 = 0.6$ kpc, $M_{\text{disk}} = 5 \times 10^{10} M_{\odot}$, and $b = 4$ kpc (similar to Smith et al. 2007). The radial potential for a spherical NFW density profile can be expressed as

$$\Phi_{\text{NFW}}(r) = -\frac{4\pi G \rho_s r_{\text{vir}}^3}{c^3 r} \ln\left(1 + \frac{cr}{r_{\text{vir}}}\right), \quad (12)$$

where c is a concentration parameter, defined as the ratio of the virial radius to the scale radius. For standard Λ CDM cosmogonies, we do not try to constrain halo flattening here. The parameter ρ_s is a characteristic density given by

$$\rho_s = \frac{\rho_{\text{cr}} \Omega_m \delta_{\text{th}}}{3} \frac{c^3}{\ln(1+c) - c/(1+c)}, \quad (13)$$

where $\rho_{\text{cr}} = 3H^2/8\pi G$ is the critical density of the universe, Ω_m is the contribution of matter to the critical density, and δ_{th} is the critical overdensity at virialization. The virial mass can then be determined from the virial radius, using

$$M_{\text{vir}} = \frac{4\pi}{3} \rho_{\text{cr}} \Omega_m \delta_{\text{th}} r_{\text{vir}}^3. \quad (14)$$

For our analysis we adopt $\Omega_m = 0.3$, $\delta_{\text{th}} = 340$, $H_o = 65 \text{ km s}^{-1} \text{ Mpc}^{-1}$. Given recent discussions of (and doubts raised) whether the baryons modify the dark matter profile, as expected from “adiabatic contraction” (Dutton et al. 2007), we consider both an unaltered and an adiabatically contracted NFW profile in the fit of Φ_{tot} .

By fitting the observed $V_{\text{cir}}(r)$ with $\sqrt{rd\Phi/dr}$ from $\Phi_{\text{tot}}(r)$ shown as Eqn.9, we can constrain the halo mass of the Milky Way. In this fit, we simply adopt an unaltered NFW profile and a present-day relation between the mean value of c and M_{vir} ,

$$\log_{10} c = 1.075 - 0.12[\log_{10} M_{\text{vir}} - 12]. \quad (15)$$

This relation is accurate over the range $11 \leq \log M_{\text{vir}} \leq 13$, and is based on the model of Macciò et al. (2007) with $\Omega_m = 0.3$, $\Omega_{\Lambda} = 0.7$, $\sigma_8 = 0.9$, and $n_i = 1.0$. Therefore the M_{vir} is

derived as a 1-parameter fit (fit only M_{vir} , presuming $c(M_{\text{vir}})$). The results are summarized in Figure 15.

Specifically, for the circular velocity estimates resulting from Steinmetz’s simulation, we find

$$M_{\text{vir}} = 1.03 \pm 0.19 \times 10^{12} M_{\odot},$$

with $r_{\text{vir}} = 278 \pm 17$ kpc and $c = 11.8$.

For the circular velocity estimates based on Naab’s simulation we find

$$M_{\text{vir}} = 0.79 \pm 0.15 \times 10^{12} M_{\odot},$$

with $r_{\text{vir}} = 255 \pm 17$ kpc and $c = 12.2$.

In above two cases we have adopted an unaltered NFW profile and an average relation between c and M_{vir} . If we fit an adiabatically contracted NFW profile (using the prescription of Blumenthal et al. 1986 and Mo et al. 1998) and the same disk and bulge as Eqn.10 and Eqn.11, taking concentration parameter (c) and virial mass (M_{vir}) of the NFW profile as independent parameters (i.e., we do not require that they follow the relationship in Eqn 15), the M_{vir} can be derived as a 2-parameter fit (M_{vir} and c) as shown in Figure 16.

For the circular velocity estimates resulting from Steinmetz’s simulation,

$$M_{\text{vir}} = 1.18 \pm 0.28 \times 10^{12} M_{\odot},$$

with $r_{\text{vir}} = 291 \pm 17$ kpc and $c = 6.3$.

The virial mass calculated by the circular velocity estimates based on Naab’s simulation,

$$M_{\text{vir}} = 1.12 \pm 0.17 \times 10^{12} M_{\odot},$$

with $r_{\text{vir}} = 286 \pm 17$ kpc and $c = 5.1$.

Note that although contracted and uncontracted halo fits differ quite strongly in their (initial) concentration, reassuringly the M_{vir} estimates remain relatively unaffected. The lower concentrations ($c \sim 6$) for the contracted halo fits are still reasonably consistent with the concentration scatter expected from cosmological simulations (e.g. NFW 96).

Note also, that the fits for the contracted and uncontracted halos match comparably well, and our data can not discriminate the two scenarios.

We have carried out an analogous procedure to Section 3.2 using $P(V_{\text{l.o.s.}}/V_{\text{esc}})$ and found lower limits on M_{vir} of $0.5 \times 10^{12} M_{\odot}$, which do not appear to be as stringent as the $V_{\text{cir}}(r)$ estimates.

5. Summary and Conclusion

We have constrained the mass distribution of the Milky Way’s dark matter halo, by analyzing the kinematics of nearly 2500 BHB stars drawn from SDSS DR-6, which reach to Galactocentric distances of ~ 60 kpc. To obtain a “clean sample” of BHB stars, we have re-analyzed all candidate BHB spectra, following the prescription by Sirko et al. 2004, which should result in a contamination fraction (mostly by BS stars) of well below 10 %. The metallicity distribution, centered on $[\text{Fe}/\text{H}] \sim -1.8$, confirms that most sample members must be halo stars. The distances to the BHB stars are known to $\sim 10\%$.

To account for the complex survey geometry and for plausible orbital distributions of those BHB stars, we have compared the observed radial velocities to analogous quantities drawn from the “stars particles” in galaxy formation simulations that resemble the Milky Way. In particular, we have placed an “observer” at 8.0 kpc from the simulation centers, looking in the actual SDSS directions and sampling radial velocities for stars that are more than 4 kpc above and below the disk plane. We then explored to what mass scale, or $V_{\text{cir}}(r)$, the simulations need to be scaled to in order to match the observed line-of-sight velocity distribution in a set of radial bins. In this analysis, we adjusted this scaling using the Jeans Equation, to account for the slight difference in the radial profile of observed halo stars ($\rho \sim r^{-3.5}$) and simulated halo stars ($\rho \sim r^{-2.9}$) over this radial range.

This procedure results in direct estimates of $V_{\text{cir}}(r)$ from ~ 10 kpc to ~ 60 kpc, the best such estimates to date over this range. The circular velocity estimate varies slightly with radius, dropping from $\sim 230\text{kms}^{-1}$ at 10 kpc to $\sim 180\text{kms}^{-1}$ in the most distant two bins. Applying this procedure to two independent cosmological simulations (T. Naab and M. Steinmetz, respectively) results in consistent estimates of $V_{\text{cir}}(r)$. The mass enclosed within 60 kpc, constrained quite directly by the data, is found to be $4.0 \pm 0.7 \times 10^{11} M_{\odot}$. A simple, Jeans Equation based modelling approach, assuming (an-)isotropics of either $\beta = 0.37$ or $\beta = 0$ (as found for the halo stars in the cosmological simulations) yields results that are consistent with these values.

Although each of the $V_{\text{cir}}(r)$ points were estimated independently, the implied overall profile is consistent with both the mass profile in the simulations and with a parameterized mass model that combines a fixed disk and bulge model with an NFW dark matter halo, whose concentration c corresponds to the expected mean value for its virial mass. We have also explored halo fits with the concentration c as a free parameter and we have explored halo profiles that have been modified by adiabatic contraction. We find that our data cannot discriminate well whether adiabatic contraction occurs or not: an uncontracted halo of higher than average concentration and a contracted halo of (initially) low concentration fit comparably well. The resulting virial masses, $M_{\text{vir}} = 1.1 \pm 0.2 \times 10^{12} M_{\odot}$, are consistent

for both fitting approaches.

We have checked that these results are quite robust with respect to distance errors, modest sample contamination ($\leq 10\%$), and the choice of a different, independent galaxy formation simulation.

M_{vir} , which does imply an extrapolation from $r_{\text{max}} = 60$ kpc to the virial radius of ~ 250 kpc, is consistent with a recent estimate from a much smaller sample of halo stars (Battaglia et al. 2006), but it is lower than previous estimates that also rely on the kinematics of satellite galaxies (e.g. Kochanek et al 1996). However, recent results on the LMC (Kallivayalil et al. 2006; Besla et al. 2007) indicate that not even the Magellanic Clouds may be bound to the Milky Way for long, posing a potential conceptual problems for the use of satellite dynamics. It should be interesting to explore what the local group timing argument implies for M31’s halo mass, given $M_{\text{MW}} \approx 1.2 \times 10^{12} M_{\odot}$.

The estimate of $M_{\text{vir}} \sim 10^{12} M_{\odot}$, together with an estimated total cold baryonic mass of $6.5 \times 10^{10} M_{\odot}$ and a global baryon mass fraction of 0.17, implies that nearly 40% of all baryons within the virial radius have cooled to form the Milky Way’s stars and (cold) gas, consistent with recent estimates for galaxies of that mass scale, based on statistical arguments.

We note that parts of our analysis have been performed under the assumption that the stellar halo of the Galaxy is considered as a single relaxed population, or one that matches the simulations. Recent evidence from Carollo et al. (2007) and Miceli et al. (2007) suggest that the halo may well be more complex, and comprise two distinct populations of inner- and outer-halo stars, with (slightly) different net rotational velocities and spatial profiles. We defer all analysis of kinematic and spatial sub-structure in this particular sample to a future paper.

Overall, SEGUE and SDSS have shown also in this context that it can provide unparalleled sets of kinematic tracers for the Milky Way, providing a direct “rotation curve” estimate of the Milky Way extending to 60 kpc. Once the full set of spectroscopy from SEGUE is available, a much larger set of stars for such an analysis should be available. The proposed extension of SDSS, known as SDSS-III (and using a more sensitive, 1000 fiber spectrograph), will provide the opportunity to obtain higher quality spectra for much fainter, and more distant BHB stars, thus extending the reach of such all analysis to over 100 kpc.

Drs. Xianzhong Zheng and Jianrong Shi are thanked for useful discussions and assistance.

This work was made possible by the support of the Chinese Academy of Sciences and the Max-Planck-Institute for Astronomy, and is supported by the National Natural Science

Foundation of China under grants Nos. 10433010 and 10521001.

TCB and YSL acknowledge partial support from the US National Science Foundation under grants AST 06-0715 and AST 07-07776, as well as from grant PHY 02-15783; Physics Frontier Center / Joint Institute for Nuclear Astrophysics (JINA).

PRF acknowledges partial support through the Marie Curie Research Training Network ELSA (European Leadership in Space Astrometry) under contract MRTN-CT-2006-033481.

Funding for the Sloan Digital Sky Survey (SDSS) and SDSS-II has been provided by the Alfred P. Sloan Foundation, the Participating Institutions, the National Science Foundation, the U.S. Department of Energy, the National Aeronautics and Space Administration, the Japanese Monbukagakusho, and the Max Planck Society, and the Higher Education Funding Council for England. The SDSS Web site is <http://www.sdss.org/>. The SDSS is managed by the Astrophysical Research Consortium (ARC) for the Participating Institutions. The Participating Institutions are the American Museum of Natural History, Astrophysical Institute Potsdam, University of Basel, University of Cambridge, Case Western Reserve University, The University of Chicago, Drexel University, Fermilab, the Institute for Advanced Study, the Japan Participation Group, The Johns Hopkins University, the Joint Institute for Nuclear Astrophysics, the Kavli Institute for Particle Astrophysics and Cosmology, the Korean Scientist Group, the Chinese Academy of Sciences (LAMOST), Los Alamos National Laboratory, the Max-Planck-Institute for Astronomy (MPIA), the Max-Planck-Institute for Astrophysics (MPA), New Mexico State University, Ohio State University, University of Pittsburgh, University of Portsmouth, Princeton University, the United States Naval Observatory, and the University of Washington.

REFERENCES

- Abadi, M. G. et al. 2003, *ApJ*, 591, 499A
- Abadi, M. G. et al. 2003, *ApJ*, 597, 21A
- Adelman-McCarthy, J. K., et al. 2007a, *ApJS*, 172, 634
- Adelman-McCarthy, J. K., et al. 2007b, submitted to *ApJS*, (arXiv: 0707.3413)
- Allende Prieto, C., et al. 2007, *AJ*, submitted
- Arnold, R. & Gilmore, G. 1992, *MNRAS*, 257, 225
- Battaglia G. et al. 2005, *MNRAS*, 364, 433

- Battaglia G. et al. 2006, MNRAS, 370, 1055
- Bell, E. F., et al. 2007, submitted to APJ, (arXiv:0706.0004)
- Binney J. & Tremaine S. 1987, Galactic Dynamics. Princeton Univ. Press, Princeton, NJ
- Blumenthal G. R., Faber S. M., Flores R., Primack J. R., 1986, ApJ, 301, 27
- Carollo, D., Beers, T.C., Y.S. Lee, Y.S., Chiba, M., Norris, J.E., Wilhelm, R., et al., 2007, Nature, 450, 1020
- Clewley, L., Warren, S. J., Hewett, P. C., Norris, J. E., Peterson, R. C., & Evans, N. W. 2002, MNRAS, 337, 87
- Dehnen W., McLaughlin D. E., & Sachania J. 2006, MNRAS, 369, 1688
- Dehnen W., & Binney J. J. 1998, MNRAS, 298, 387
- Dutton A.A., van den Bosch F.C., Dekel A., Courteau S., 2007, ApJ, 654, 27
- Flynn, C., Sommer-Larsen, J., & Christensen, P. R. 1994, MNRAS, 267, 77
- Fukugita, M., Ichikawa, T., Gunn, J. E., Doi, M., Shimasaku, K., & Schneider, D. P. 1996, AJ, 111, 1748
- Gunn, J.E., et al. 1998, AJ, 116, 3040
- Gunn, J.E., et al. 2006, AJ, 131, 2332
- Hernquist L., 1990, ApJ, 356, 359
- Hogg, D.W., Finkbeiner, D.P., Schlegel, D.J., & Gunn, J.E. 2001, AJ, 122, 2129
- Ivezic, Z., et al. 2004, AN, 325, 583
- Kinman, T. D., Suntzeff, N. B., & Kraft, R. P. 1994, AJ, 108, 1722
- Klypin A., Zhao H., & Somerville R. 2002, ApJ, 573, 597
- Kulessa A. S. & Lynden-Bell D. 1992, MNRAS, 310, 105
- Kochanek C. S. 1996, ApJ, 547, 228 (K96)
- Lee, Y.S., et al. 2007a, AJ, submitted
- Lee, Y.S., et al. 2007b, AJ, submitted

- Lindgren L., & Perryman M. A. C. 1987, ApJ, 320, 493
- Little B., & Tremaine S. D. 1987, ApJ, 320, 493
- Lupton, R., Gunn, J. E., Ivezić, Z., Knapp, G. R., & Kent, S. 2001, *Astronomical Data Analysis Software and Systems X*, 238, 269
- Maccio A.V., Dutton A.A., van den Bosch F.C., Moore B., Potter D., Stadel J., 2007, MNRAS, 378, 55
- Miceli, A., Rest, A., Stubbs, C. W., Hawley, S. L., Cook, K. H., Magnier, E. A., et al., (2007) ApJ, in press (arXiv:0706.1583).
- Mo H. J., Mao S. D., White S. D. M., 1998, MNRAS, 295, 319
- Munn, J. A., et al. 2004, AJ, 127, 3034
- Naab, T., et al. 2007, ApJ, 658, 710N
- Navarro J. F., Frenk C. S., & White S. D. M., 1996, ApJ, 462, 563
- Newberg, H. J.; Sloan Digital Sky Survey Collaboration, AAS, 20311211N
- Pier, J. R. 1983, ApJS, 53, 791
- Pier, J. R., Munn, J. A., Hindsley, R. B., Hennessy, G. S., Kent, S.M., Lupton, R. H., & Ivezić, Z. 2003, AJ, 125, 1559
- Sakamoto T., Chiba M., & Beers T. C. 2003, A&A, 397, 899
- Schlegel, D., Finkbeiner, D., & Davis, M. 1998, ApJ, 500, 525
- Sérsic, J. L. 1968, *Atlas de galaxies australes* Cordoba, Argentina: Observatorio Astronomico
- Sirko, E. et al. 2004, AJ, 127, 899
- Smith, J. A., et al. 2002, AJ, 123, 2121
- Smith, M. C. et al. 2007, MNRAS, 379, 755S
- Sommer-Larsen, J. & Christensen, P. R. 1986, MNRAS, 219, 537
- Springel, V. 2005, MNRAS, 364, 1105s
- Springel, V. & Hernquist, L. 2003, MNRAS, 339, 289s

Steinmetz, M. et al. 2006, AJ, 132, 1645

Stoughton, C., et al. 2002, AJ, 123, 485

Tucker, D., et al. 2006, AN, 327, 821

Unwin, Stephen C. & Shao, Michael 2000, SPIE, 4006, 754u

Wilkinson M. I., & Evans N. W., 1999, MNRAS, 310, 645

Wilhelm, R., Beers, T. C., & Gray, R. O. 1999, AJ, 117, 2308

York, D. G. et al. 2000, AJ, 120, 1579

Zaritsky D., Olszewski E. W., Schommer R. A., Peterson R. C., & Aaronson M. 1989, ApJ, 345, 759

Table 1: Estimates of the circular velocities as a function of distance.

r (kpc)	$V_{\text{cir,N}}$ (km s $^{-1}$)	$V_{\text{cir,S}}$ (km s $^{-1}$)
7.5	216 \pm 22	201 \pm 22
12.5	227 \pm 22	235 \pm 22
17.5	179 \pm 22	205 \pm 22
22.5	168 \pm 22	173 \pm 22
27.5	183 \pm 27	168 \pm 27
32.5	143 \pm 23	173 \pm 23
37.5	170 \pm 38	172 \pm 38
42.5	183 \pm 34	200 \pm 34
47.5	165 \pm 33	146 \pm 33
55.0	183 \pm 32	193 \pm 32

Note. — $V_{\text{cir,N}}$ denote the estimates based on Naab’s simulation, while $V_{\text{cir,S}}$ denote the estimates based on Steinmetz’s simulation. These estimates have been derived from the velocity scaling of the observed distribution that yields the best agreement to the simulated velocity distribution, as determined by the K-S test probability. See text for further information.

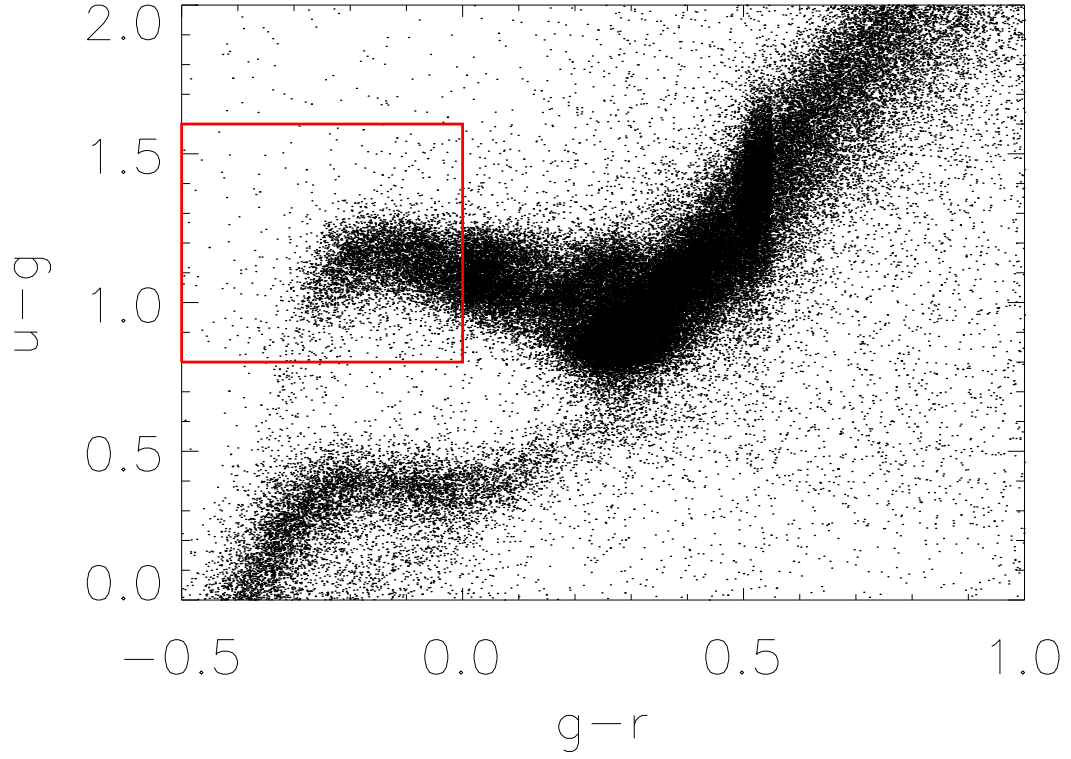


Fig. 1.— SDSS color-color diagram showing all spectroscopically targeted objects that were subsequently confirmed as stars. The main sequence runs from the center of this diagram towards the upper right, and the large Balmer jump of A-colored stars places them in the offshoot, where our “color cut” selection box is drawn. This color selection approach follows Yanny et al (2000).

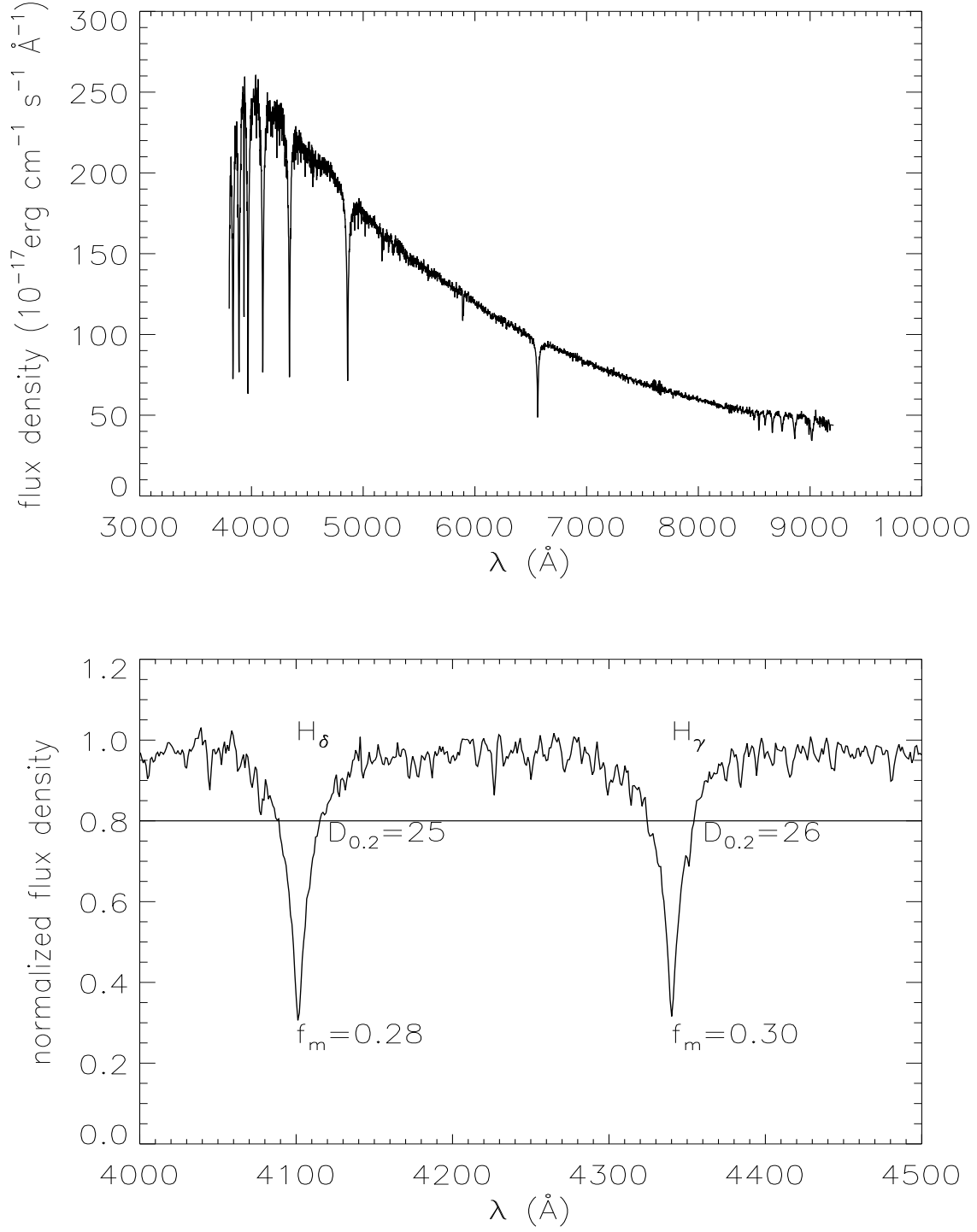


Fig. 2.— Spectrum of a typical (high-S/N) BHB star (upper panel), and the $H_\gamma \sim H_\delta$ region of the same star with the continuum divided out (lower panel). The parameters ($f_m, D_{0.2}$) that are used for the sample selection are labelled for both lines (see Section 2.1.2 for discussion).

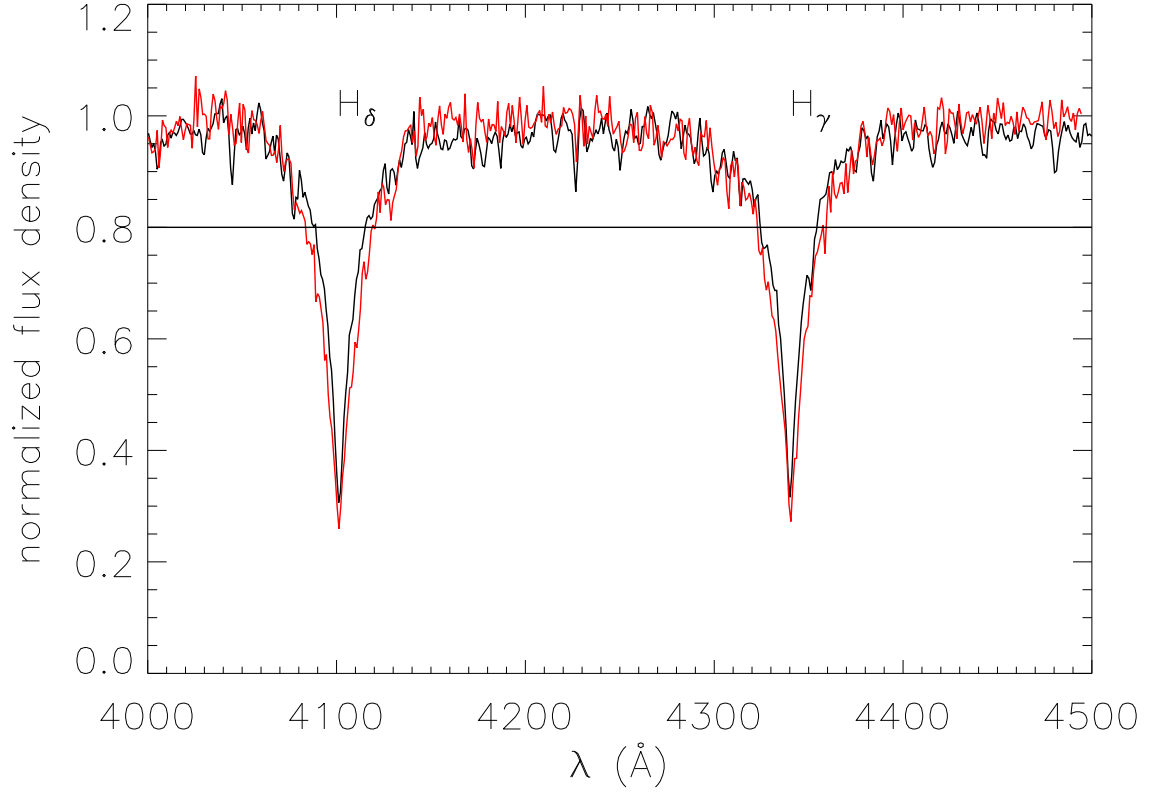


Fig. 3.— Normalized spectrum of a BHB star (black line) and a BS star (red line), of similar effective temperatures, in the $H_\gamma \sim H_\delta$ region. Although subtle, one can note that the BS stars’s Balmer lines are wider at 20% below the local continuum, and that it does not extend to the same depth below the continuum as the BHB star. Both effects arise due to the higher gravity of the BS star.

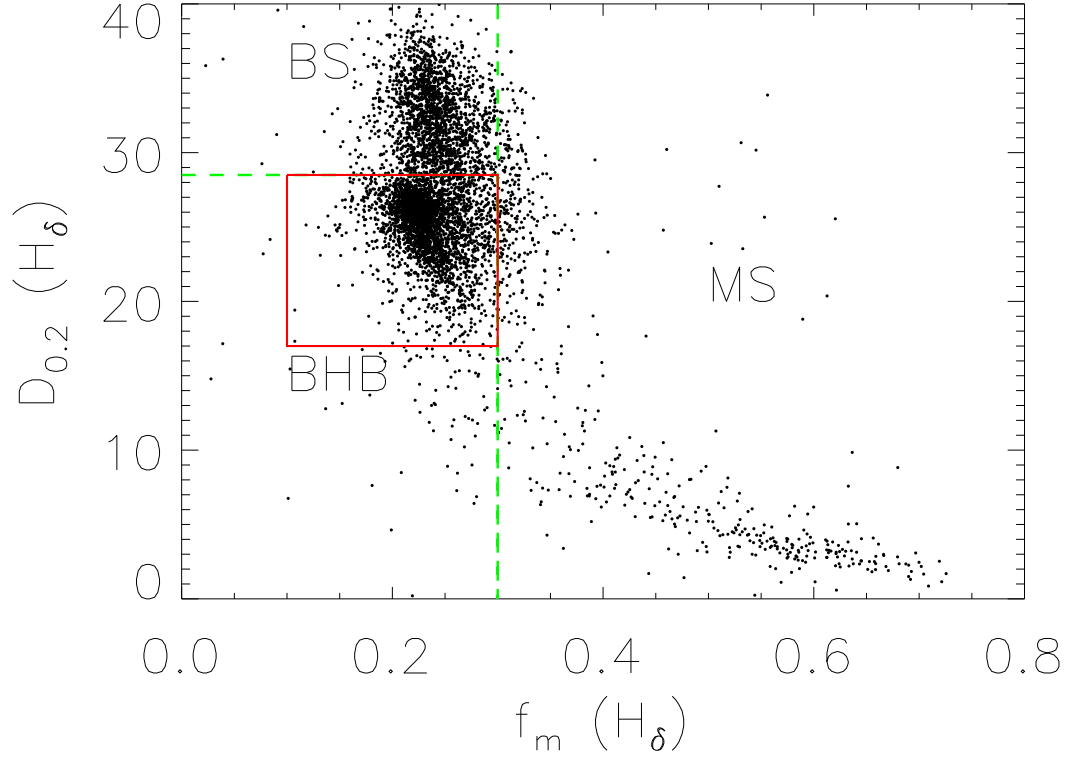


Fig. 4.— The parameters f_m and $D_{0.2}$, as determined from the H_{δ} line, for stars that pass the color cuts shown in Figure 1. The trail of stars with $f_m \geq 0.35$ are too cool to be BHB stars, while the concentration of stars with $D_{0.2} \geq 28.5\text{\AA}$ is due to blue stragglers with higher surface gravity. The stars that lie well outside the main locus are poor parameter determinations due to missing spectroscopic data at the location of the H_{δ} line. The region enclosed by the red box is used as the BHB selection criterion for the H_{δ} $D_{0.2}$ & f_m method.

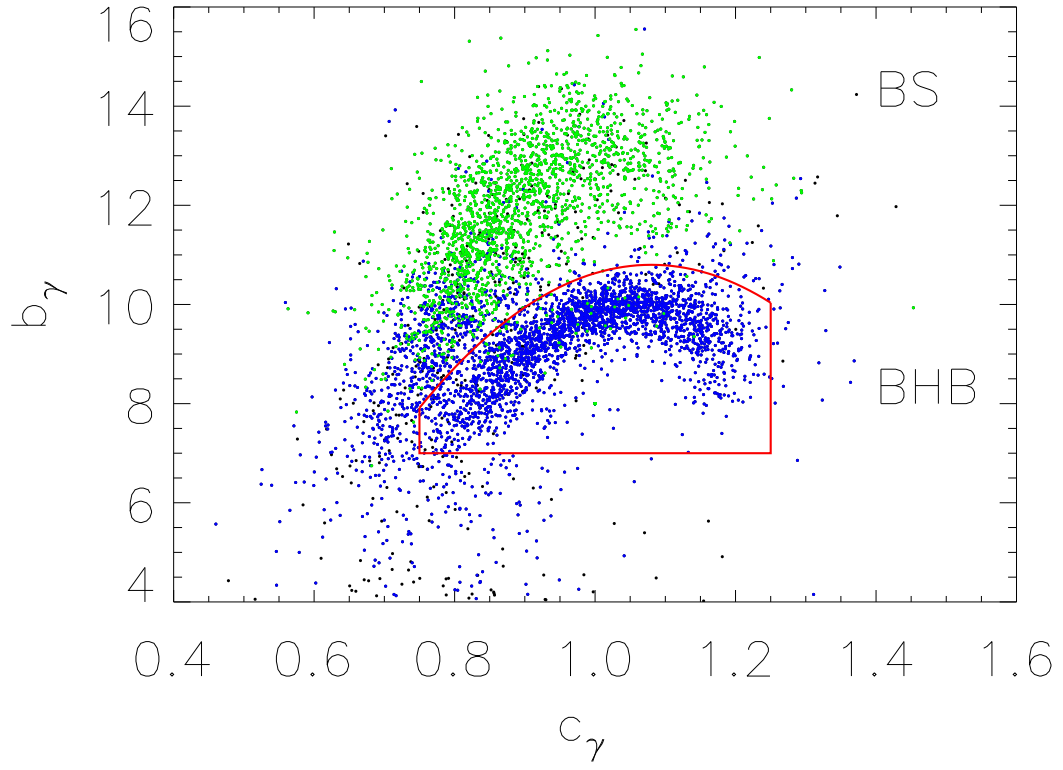


Fig. 5.— Green dots are BS stars and blue dots are BHB stars identified by the $D_{0.2}$ & f_m method. They can be distinguished clearly by the “gap”. The black dots are MS stars. The closed region indicates the H_γ scale width-shape criteria that selects BHB stars.

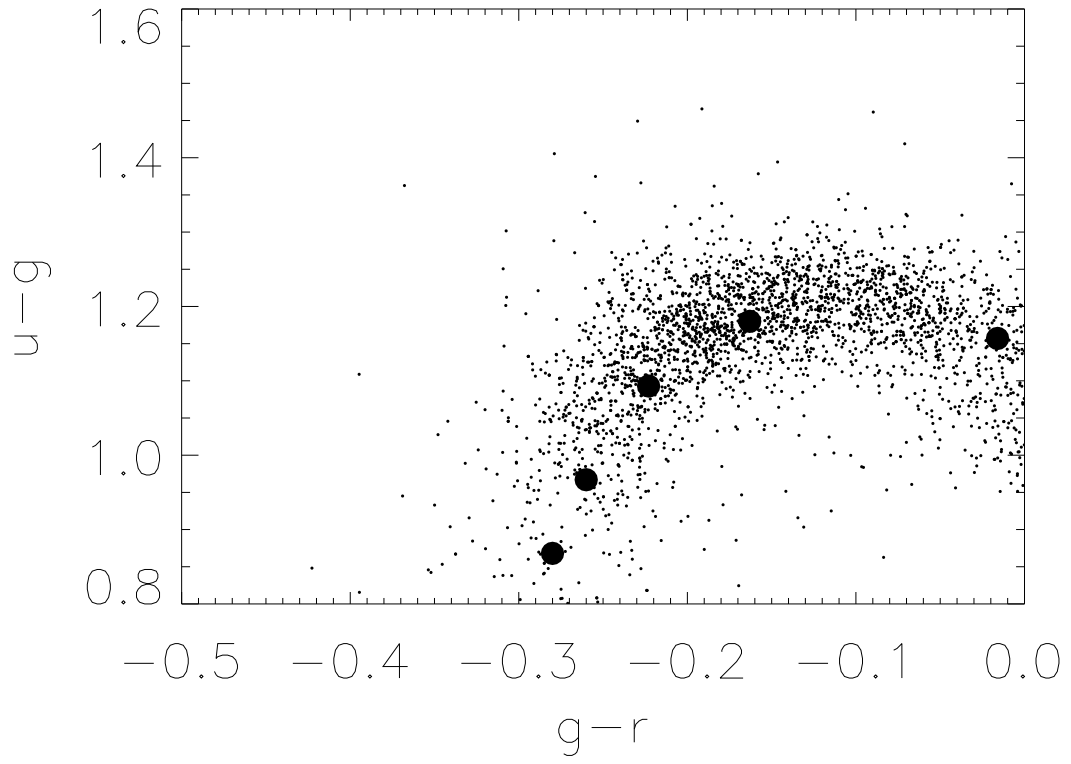


Fig. 6.— Color-color ($g-r$ vs. $r-g$) diagram of our BHB stars. The five black dots, starting from the right to the left, represent the model colors for BHB stars of absolute magnitudes $M_g = 0.60, 0.55, 0.65, 0.70, 0.80$.

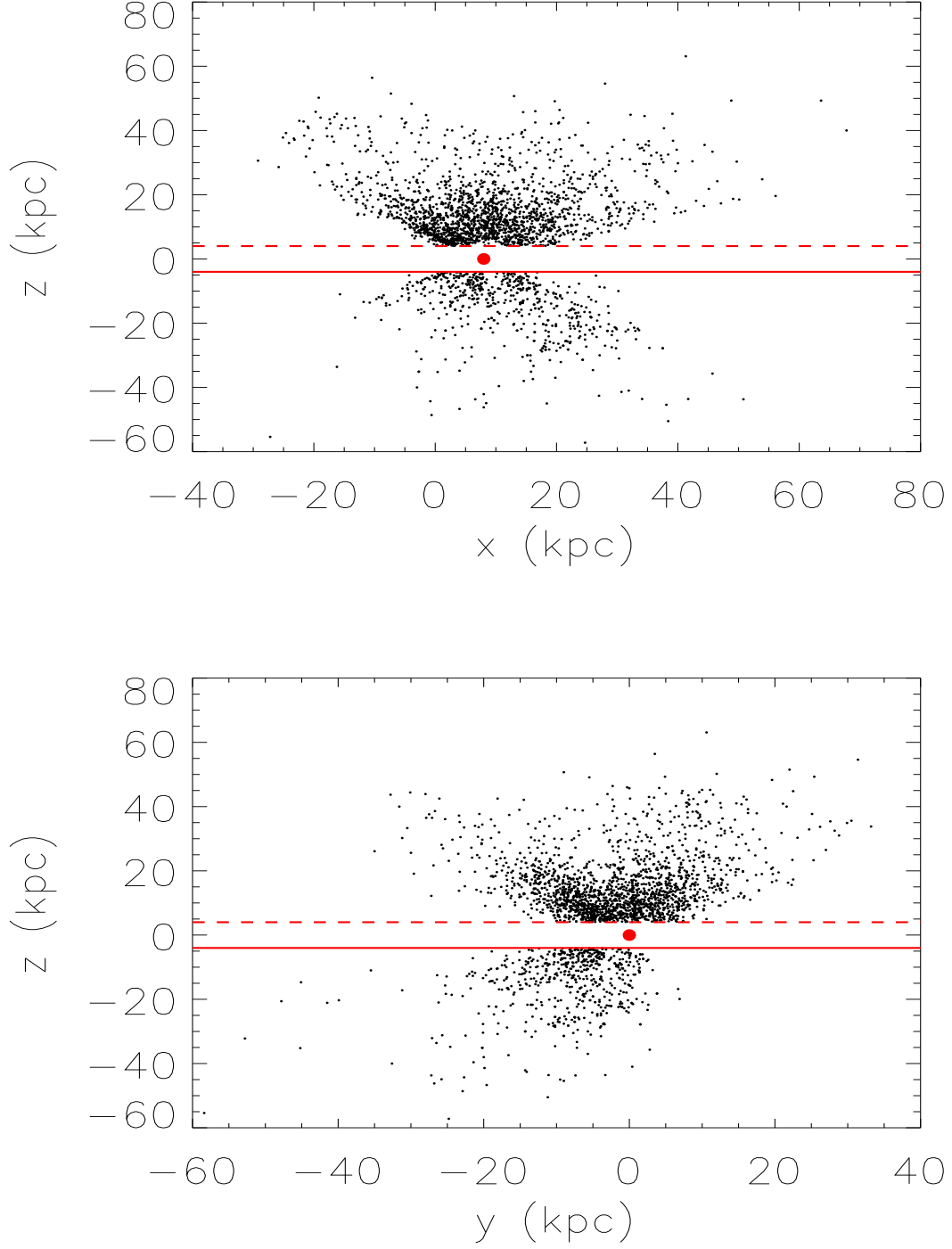


Fig. 7.— The spatial distribution of the BHB stars in our sample, projected in the z - x (upper panel) and z - y plane (lower panel), respectively. The red dot is the Sun; the red solid and dashed lines are the planes 4 kpc below and above the Galactic disk plane.

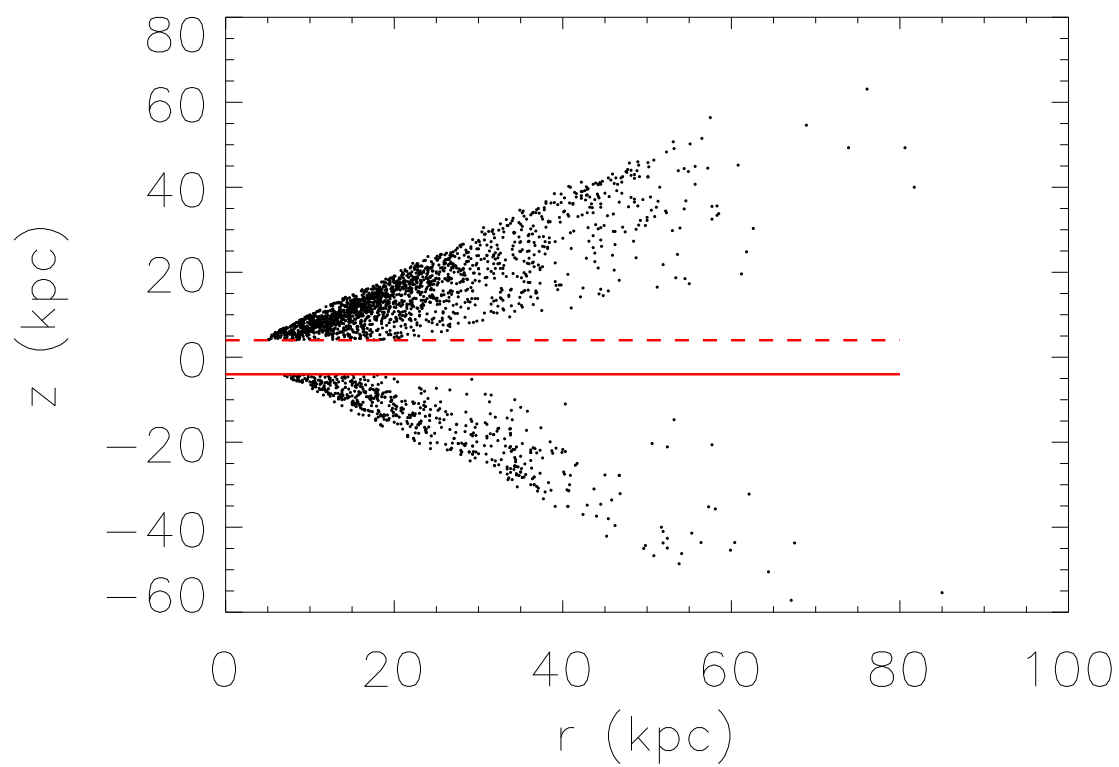


Fig. 8.— The spatial distribution of the sample BHB stars in the z - r plane. The coordinate origin is the location of the Galactic center. Red solid and dashed lines are the planes 4 kpc below and above the Galactic disk plane.

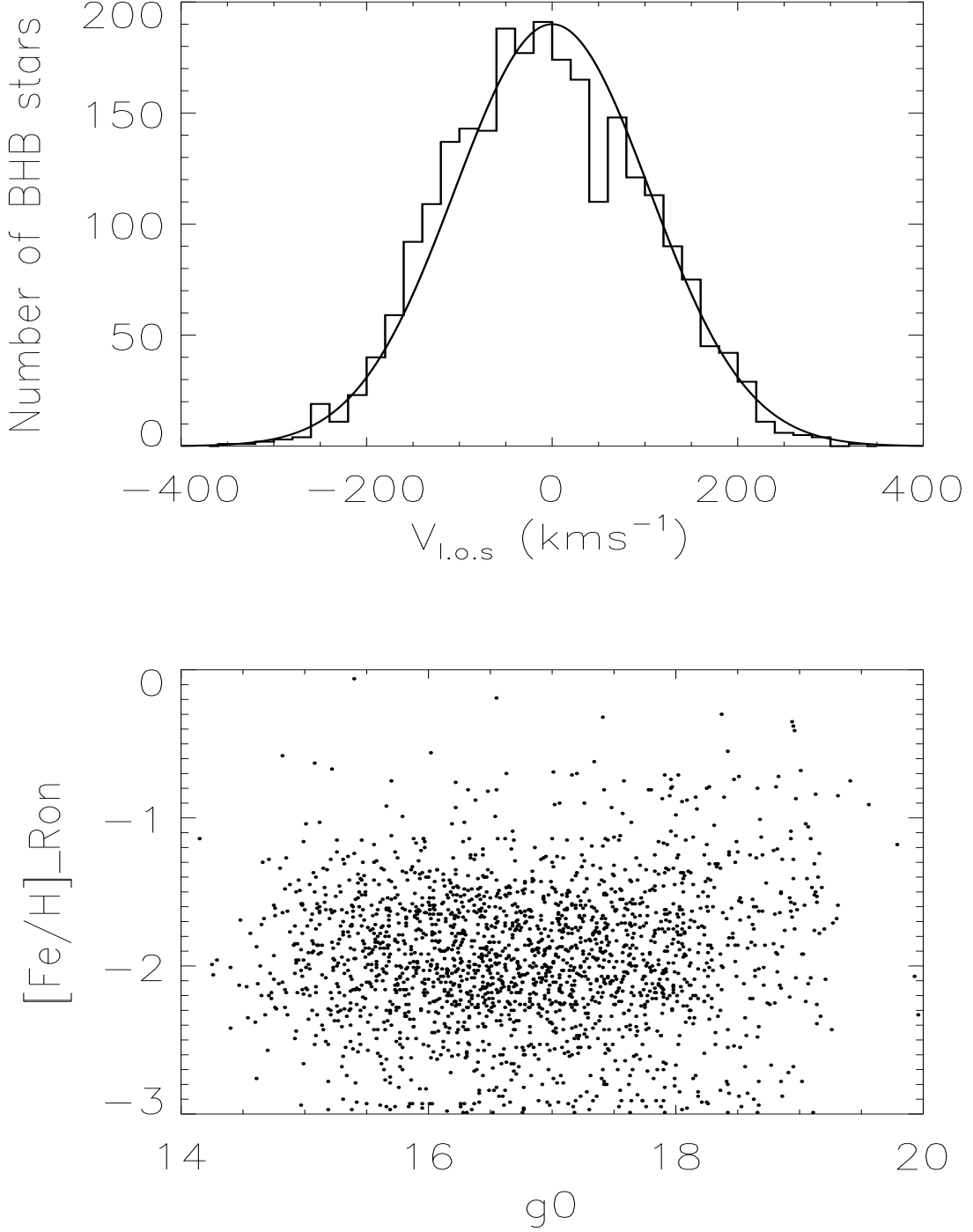


Fig. 9.— (Upper panel) The distribution of line-of-sight velocities, corrected to the GSR, for the entire sample of BHB stars. A Gaussian of width $\sigma = 106 \text{ km s}^{-1}$ centered on the local standard of rest is shown for reference. (Lower panel) The distribution of metallicities, $[\text{Fe}/\text{H}]$, as a function of apparent magnitude, for the entire sample of halo BHB stars.

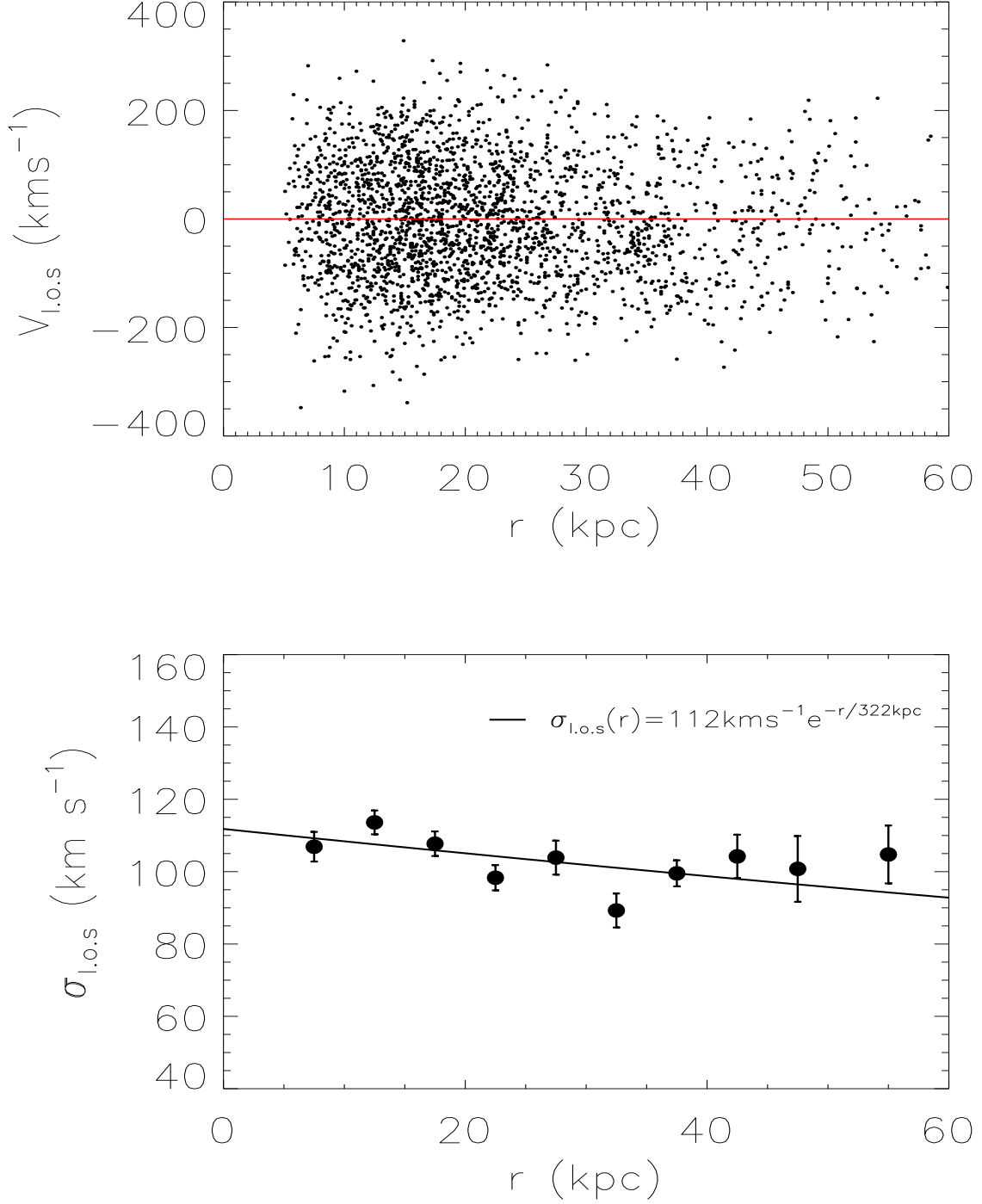


Fig. 10.— (Upper panel) The distribution of $V_{l.o.s}$ as a function of Galactocentric distance, r , for the entire sample of halo BHB stars. (Lower panel) The velocity dispersion, $\sigma_{l.o.s}$, as a function of Galactocentric distance. A best fit exponentially falling relationship is plotted.

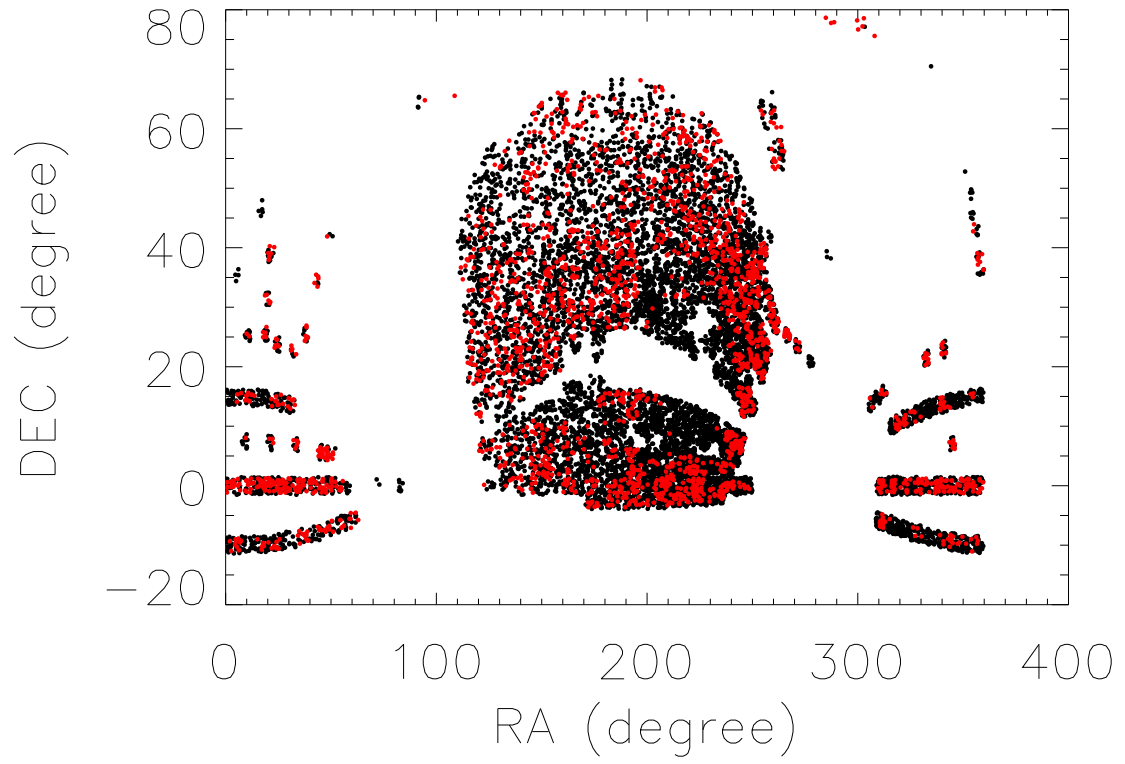


Fig. 11.— The RA & DEC distribution of the observed BHB stars (red dots) and selected simulated stars (black dots), drawn from the simulation by T. Naab.

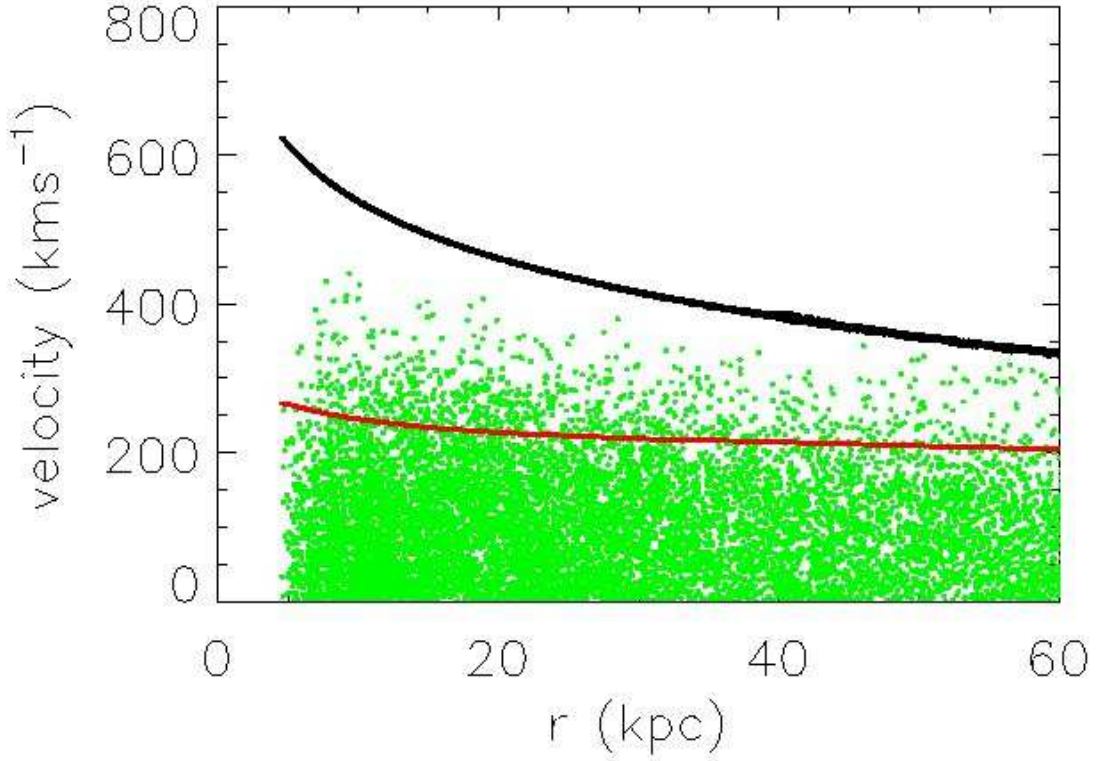


Fig. 12.— The Galactocentric radial velocity distribution of the stars in T. Naab’s simulation (see Section 3) with the same geometric selection as the data (red dots); the simulations are “viewed” from the position of the Sun to lie within the SDSS DR-6 footprint. The black line delineates the predicted escape velocity, while the blue line indicates the predicted circular velocity.

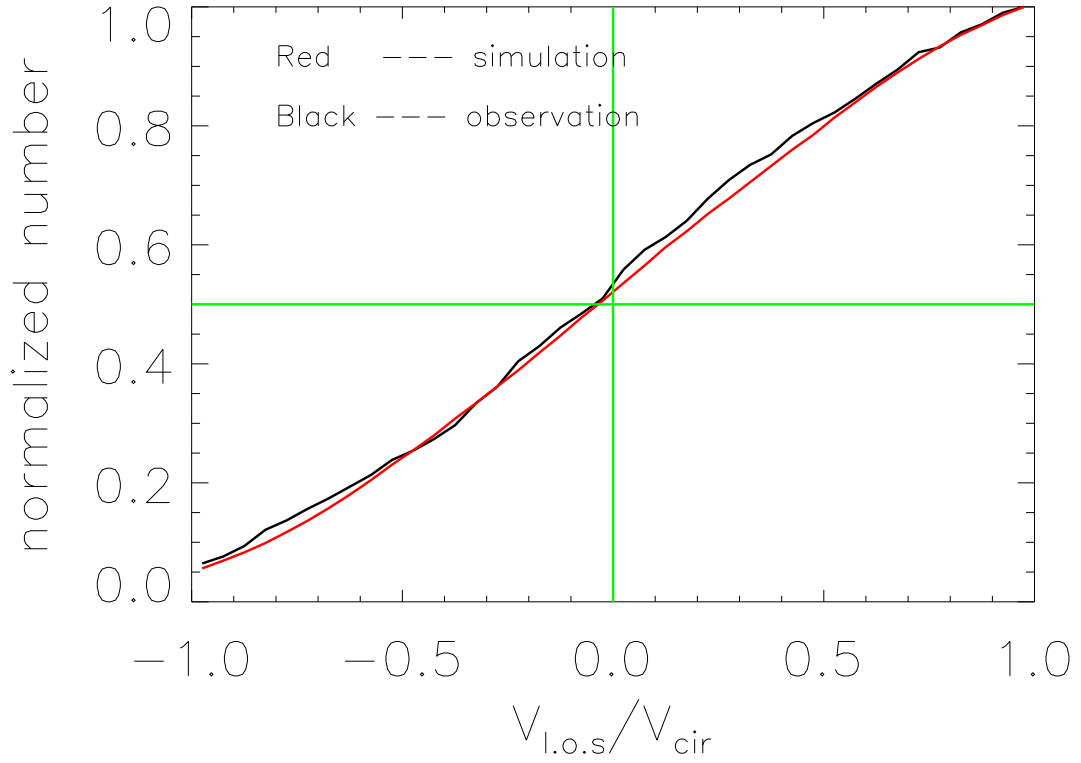


Fig. 13.— Comparison of the Galactocentric line-of-sight velocity distribution, $P(V_{\text{l.o.s.}}/V_{\text{cir}})$ between the halo star particles in the simulation by T. Naab. and the observations, shown here for radius bin $[15, 20]$ kpc. The red line is $P(V_{\text{l.o.s.,sim}}/V_{\text{cir}})$, and the black line is $P(V_{\text{l.o.s.,obs}}/V_{\text{cir}})$, after finding the best matching velocity scaling, $V_{\text{cir}} = 163 \text{ km s}^{-1}$.

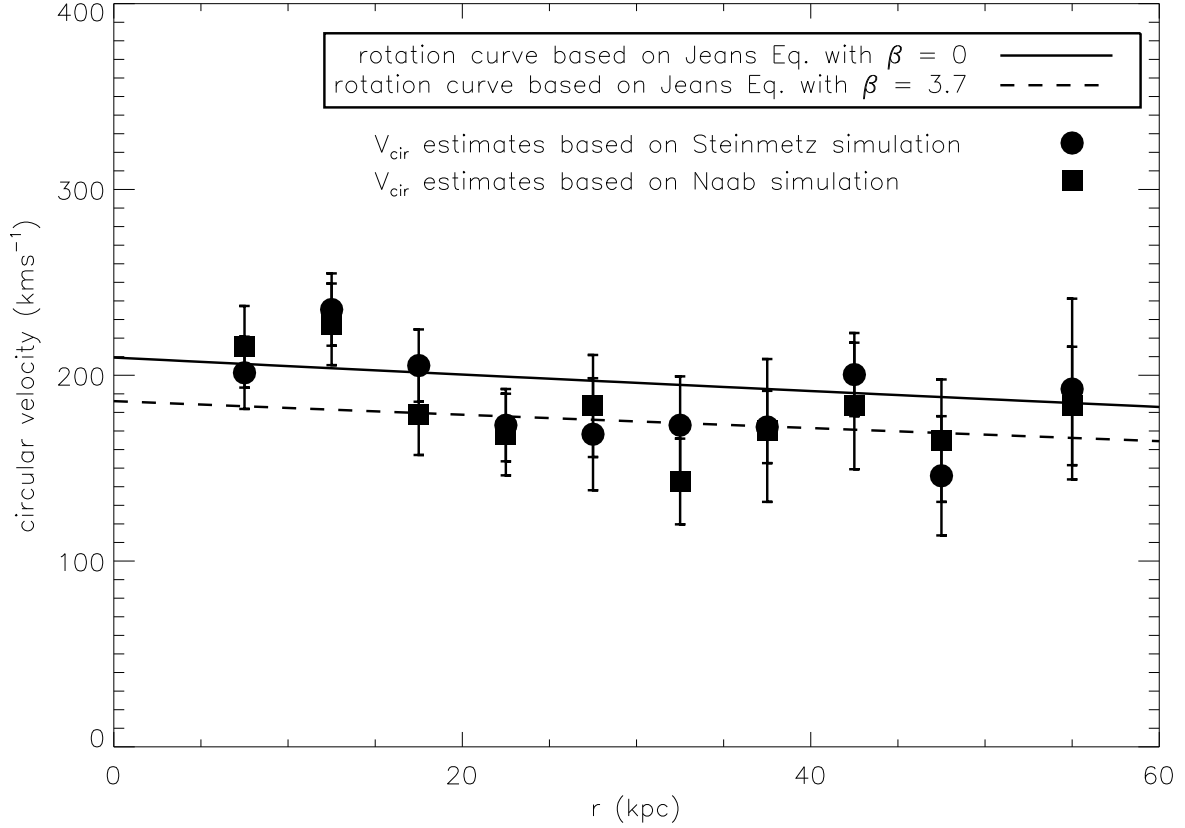


Fig. 14.— The distribution of circular velocity estimates, V_{cir} , for two different simulated galaxies. The filled circles are the V_{cir} estimates for the observed halo BHB stars based on M. Steinmetz’s simulation and the filled squares are the V_{cir} estimates based on T. Naab’s simulation. The two lines are the rotation curve estimates derived from the velocity dispersion profile (Figure 10) and the Jeans Equation with $\beta = 0.37$ and $\beta = 0$.

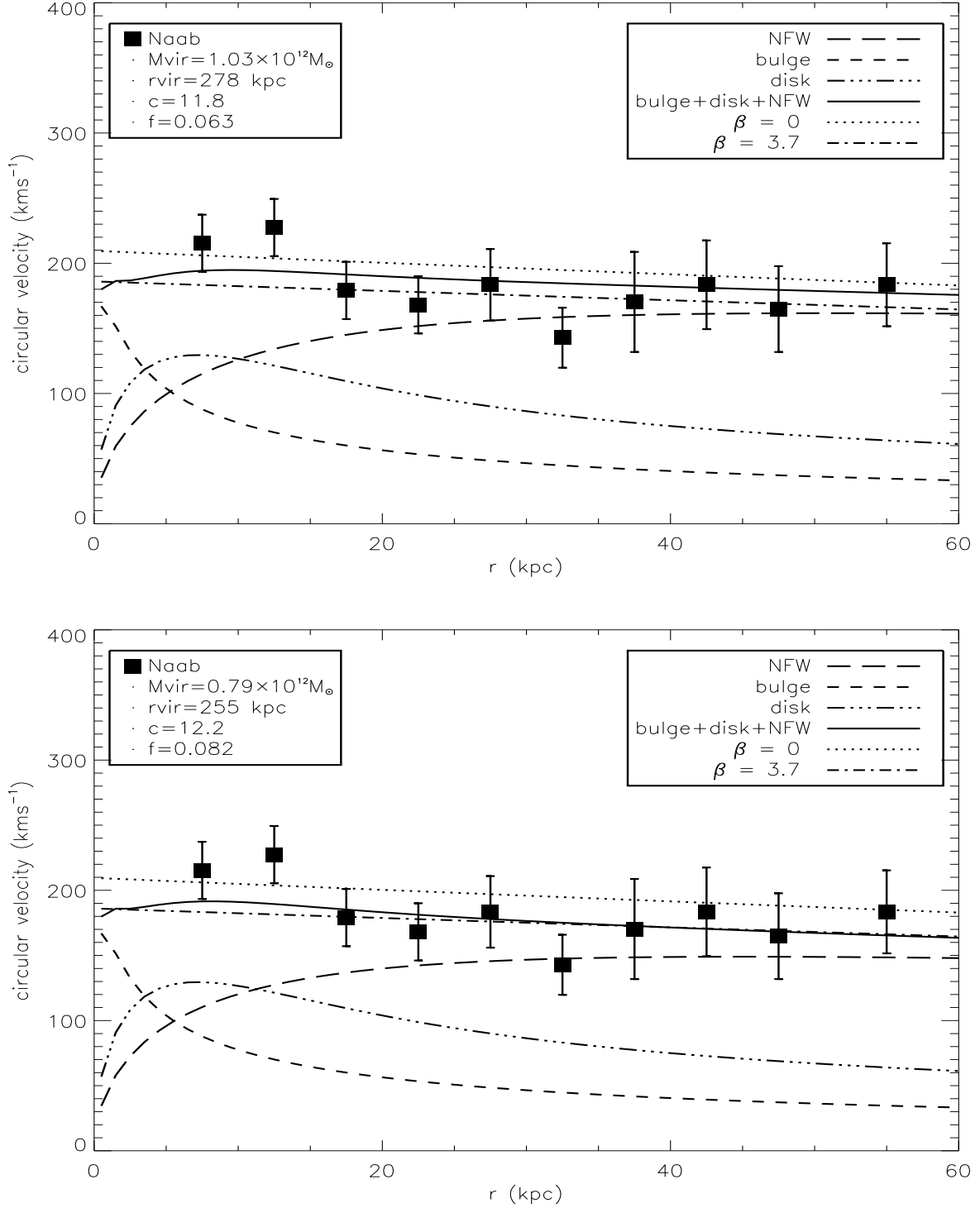


Fig. 15.— Rotation curve estimates matched by a combination of a stellar bulge, disk and an unaltered NFW dark matter profile. The solid line is the best-fit rotation curve to the $V_{\text{cir}}(r)$ estimates, while the large symbols in the two plots are the $V_{\text{cir}}(r)$ estimates. Contributions of the adopted model components (i.e. disk, bulge, and halo) and the rotation curves based on the Jeans Equation are plotted in different linestyles. Estimates of virial mass, M_{vir} , virial radius, r_{vir} , concentration parameter, c , and baryon fraction, f , are labeled in the legend.

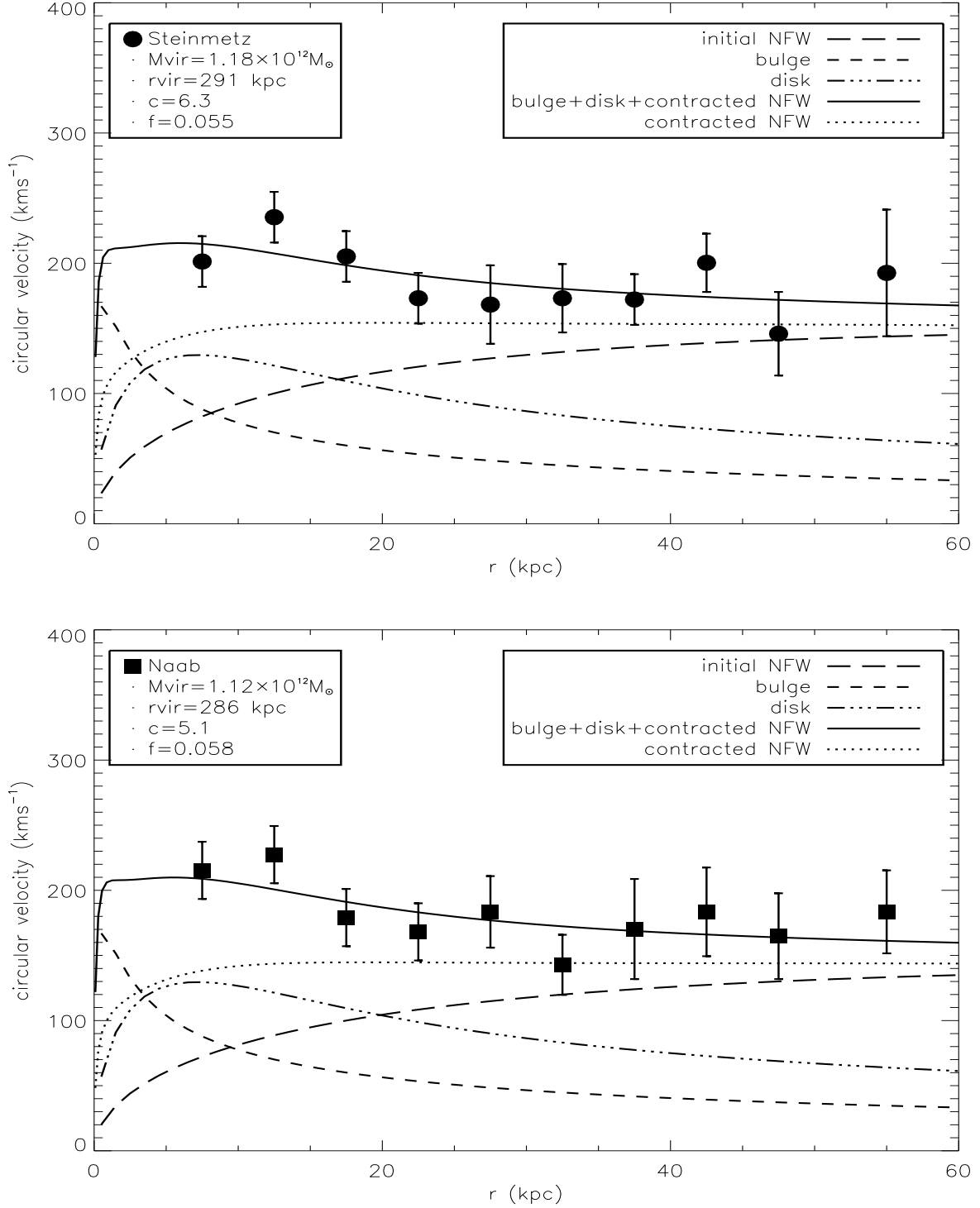


Fig. 16.— As Figure 15, but here rotation curves were derived under the assumption of a contracted NFW profile. The solid line is the best-fit rotation curve to the $V_{\text{cir}}(r)$ estimates, while the large symbols in the two plots are the $V_{\text{cir}}(r)$ estimates. Contributions of the adopted model components (i.e. disk, bulge, and halo) are plotted in different linestyles. Estimates of virial mass, M_{vir} , virial radius, r_{vir} , concentration parameter, c , and baryon fraction, f , are labeled on the plots.